arXiv:1001.1606v1 [astro-ph.CO] 11 Jan 2010

Submitted to *The Astrophysical Journal*

Timing Signatures of the Internal-Shock Model for Blazars

M. Böttcher[1] and C. D. Dermer[2]

ABSTRACT

We investigate the spectral and timing signatures of the internal-shock model for blazars. For this purpose, we develop a semi-analytical model for the time-dependent radiative output from internal shocks arising from colliding relativistic shells in a blazar jet. The emission through synchrotron and synchrotron-self Compton (SSC) radiation as well as Comptonization of an isotropic external radiation field are taken into account. We evaluate the discrete correlation function (DCF) of the model light curves in order to evaluate features of photon-energy dependent time lags and the quality of the correlation, represented by the peak value of the DCF. The almost completely analytic nature of our approach allows us to study in detail the influence of various model parameters on the resulting spectral and timing features. This paper focuses on a range of parameters in which the γ-ray production is dominated by Comptonization of external radiation, most likely appropriate for γ-ray bright flat-spectrum radio quasars (FSRQs) or low-frequency peaked BL Lac objects (LBLs). In most cases relevant for FSRQs and LBLs, the variability of the optical emission is highly correlated with the X-ray and high-energy (HE: 100 MeV) γ-ray emission. Our baseline model predicts a lead of the optical variability with respect to the higher-energy bands by 1 – 2 hours and of the HE γ-rays before the X-rays by about 1 hour. We show that variations of certain parameters may lead to changing signs of inter-band time lags, potentially explaining the lack of persistent trends of time lags in most blazars.

Subject headings: galaxies: active — gamma-rays: theory — radiation mechanisms: non-thermal

[1]Astrophysical Institute, Department of Physics and Astronomy, Clippinger 339, Ohio University, Athens, OH 45701, USA

[2]Naval Research Laboratory, Code 7653, Washington, D.C. 20375

1. Introduction

Blazars, a class of active galactic nuclei (AGNs) comprised of Flat-Spectrum Radio Quasars (FSRQs) and BL Lac objects, exhibit some of the most violent high-energy phenomena observed in AGNs to date. Their spectral energy distributions (SEDs) are characterized by non-thermal continuum spectra with a broad low-frequency component in the radio – UV or X-ray frequency range and a high-frequency component from X-rays to γ-rays. They show rapid variability across the electromagnetic spectrum. In extreme cases, the very-high-energy (VHE) γ-ray emission of blazars has been observed to vary on time scales of just a few minutes (Albert et al. 2007; Aharonian et al. 2007).

The flux variability of blazars is often accompanied by spectral changes. Typically, the flux is most rapidly variable at the high-frequency ends of the two broad spectral components of the blazar SED. In the case of quasars, this refers to the optical (B-band) to UV and MeV to GeV γ-ray bands, while in the case of high-frequency peaked BL Lac objects (HBLs) it is the X-ray and VHE γ-ray regimes where the variability is the most extreme. In a few HBLs, the X-ray spectral variability could occasionally be characterized by spectral hysteresis, i.e., a loop track of the blazar's state in a hardness-intensity diagram (e.g. Takahashi et al. 1996; Kataoka et al. 2000; Fossati et al. 2000; Zhang et al. 2002), although even within the same object this feature tends not to be persistent over multiple observations. Also in other types of blazars, hints of time lags between different observing bands are occasionally found in individual observing campaigns (e.g., Böttcher et al. 2007; Horan et al. 2009), but the search for time-lag patterns persisting throughout multiple years has so far remained unsuccessful (see, e.g. Hartman et al. 2001, for a systematic search for time lags between optical, X-ray and γ-ray emission in the quasar 3C279).

In the framework of relativistic jet models, the low-frequency (radio – optical/UV) emission from blazars is interpreted as synchrotron emission from nonthermal electrons in a relativistic jet. The high-frequency (X-ray – γ-ray) emission could either be produced via Compton upscattering of low frequency radiation by the same electrons responsible for the synchrotron emission (leptonic jet models; for a recent review see, e.g., Böttcher 2007), or due to hadronic processes initiated by relativistic protons co-accelerated with the electrons (hadronic models, for a recent discussion see, e.g., Mücke & Protheroe 2001; Mücke et al. 2003). Leptonic models have been considered in a time-dependent manner with the aim of reproducing simultaneously the SEDs and light curve features of blazars (see, e.g., Kirk, Rieger, & Mastichiadis 1998; Georganopoulos & Marscher 1998; Chiaberge & Ghisellini 1999; Kataoka et al. 2000; Kusunose, Takahara & Li 2000; Li & Kusunose 2000; Böttcher & Chiang 2002; Joshi & Böttcher 2007). The time-dependent analysis of homogeneous single-zone leptonic models showed that spectral hysteresis patterns can be reproduced in a scenario of

gradual particle acceleration and subsequent radiative cooling, and that the presence and direction of hysteresis patterns depends on the relative values of the time scales for particle acceleration, escape, and radiative cooling (Dermer 1998; Chiaberge & Ghisellini 1999).

Homogeneous leptonic jet models have met with remarkable success explaining the SEDs and correlated variability in many blazars. However, several recent observational results have seriously challenged homogeneous models and have motivated the consideration of inhomogeneous jet models. These observations include the uncorrelated variability between X-rays and γ-rays in the HBLs 1ES1959+650 (Krawczynski et al. 2004) and Mrk 421 (Błażejowski et al. 2005), and the uncorrelated optical and TeV emissions in PKS 2155-304, while X-rays and TeV γ-rays were well correlated (Costamante 2008). A particularly well motivated inhomogeneous blazar model is the internal shock model (e.g. Spada et al. 2001; Sokolov, Marscher & McHardy 2004; Mimica et al. 2004; Graff et al. 2008). In this model, the central engine is intermittently ejecting shells of relativistic plasma at varying speeds, which subsequently collide. Such models have had remarkable success in explaining SEDs and time lag features of generic blazars and deserve further study.

The realistic treatment of radiation transfer in an internal-shock model for a blazar requires the time-dependent evaluation of retarded radiation fields originating from all parts of the shocked regions of the jet. The model system is therefore highly non-linear and can generally only be solved using numerical simulations (e.g., Sokolov, Marscher & McHardy 2004; Mimica et al. 2004; Graff et al. 2008; Joshi 2009). As the current detailed internal-shock models employ either full expressions or accurate approximations to the full emissivities of synchrotron and Compton emission, a complete simulation of the time-dependent spectra and light curves is time-consuming and does therefore generally not allow to efficiently explore a large parameter space. General patterns of the SED, light curves and expected time lags between different wavelength bands have been demonstrated for very specific, but observationally very poorly constrained, sets of parameters.

For this reason, we here develop a simplified internal-shock model in which the time-dependent synchrotron and external-Compton (EC) spectra are calculated completely analytically, and the SSC emission is reduced to a two-dimensional integral to be performed numerically. This approach allows us to calculate time-dependent snapshot spectra and light curves within a few minutes, and scan a large parameter space for the resulting spectral and timing features.

Observational data of blazars often have limited, incomplete, and irregular time sampling, which complicates the evaluation of inter-band time lags and cross-correlations. The routinely used analysis method designed to overcome these problems is the discrete correlation function (DCF, see Edelson & Krolik 1988). Therefore, in order to produce results

directly comparable to observations, we subject our simulated light curves to the same DCF technique, and evaluate predicted inter-band time lags and the quality of the correlations, as represented by the peak values of the DCF.

We describe the general outline of our model in §2. The dynamics of particle acceleration and cooling, and the resulting space- and time-dependent particle distributions, will be derived in §3. In §4 we describe our evaluation of the time-dependent radiative output from the internal-shock model. We present and discuss the results of a general parameter study in §5, and conclude in §6. The appendices contain some details of the rather cumbersome analytical integrations required to evaluate the radiative output.

2. Model Setup and Shell Dynamics

We follow the collision of two relativistically moving shells (labeled a and b) in a blazar jet, powered by an intermittent central source. The basic geometry is illustrated in Fig. 1. (For a related treatment of a relativistic shell interacting with a shell of material at rest, see Dermer 2008) The two shells are being ejected from the central engine with Lorentz factors $\Gamma_{a,b}$ with $\Gamma_b > \Gamma_a \gg 1$ and associated normalized velocities $\beta_{a,b}$ (with $\beta = v/c$). In the rest-frame of the central engine, the ejection events of the two shells last for a time $\Delta t_{a,b}$. Consequently, the shells have widths (in the central-engine rest frame) of $\Delta r_{a,b} = c\beta_{a,b}\Delta t_{a,b}$. This assumes that the shells do not spread along or transverse to the direction of motion. The former effect can be important at $r_{a,b} \gtrsim \Gamma_{a,b}^2 c\Delta t_{a,b}$ (e.g., Meszaros et al. 1993), but is neglected because of the short duration of the collision during which the shell can be approximated as having a nearly constant thickness. Sideways expansion of the jet can also be neglected because of the short duration of the collision (this effect can be important for narrow decelerating jets; see e.g., Sari et al. 1999). This latter assumption is also supported by observations of extragalactic jets remaining well collimated out to kpc scales. If this assumption is valid, the shell dynamics will not depend on the time between the shell ejections.

Assuming that before the collision, the kinetic energy of the plasma in the shells' rest frames is negligible compared to the bulk kinetic energy ("cold plasma"), the kinetic luminosity of the shells is given by $L_{a,b} = \Gamma_{a,b}\dot{M}_{a,b}c^2$. This yields particle densities in the shells of

$$n'_{a,b} = \frac{L_{a,b}}{\pi R^2\, \beta_{a,b}\Gamma_{a,b}^2\, m_p c^3} \tag{1}$$

where R is the cross-sectional radius of the jet (and hence the shells), and the prime denotes quantities in the shell rest frame.

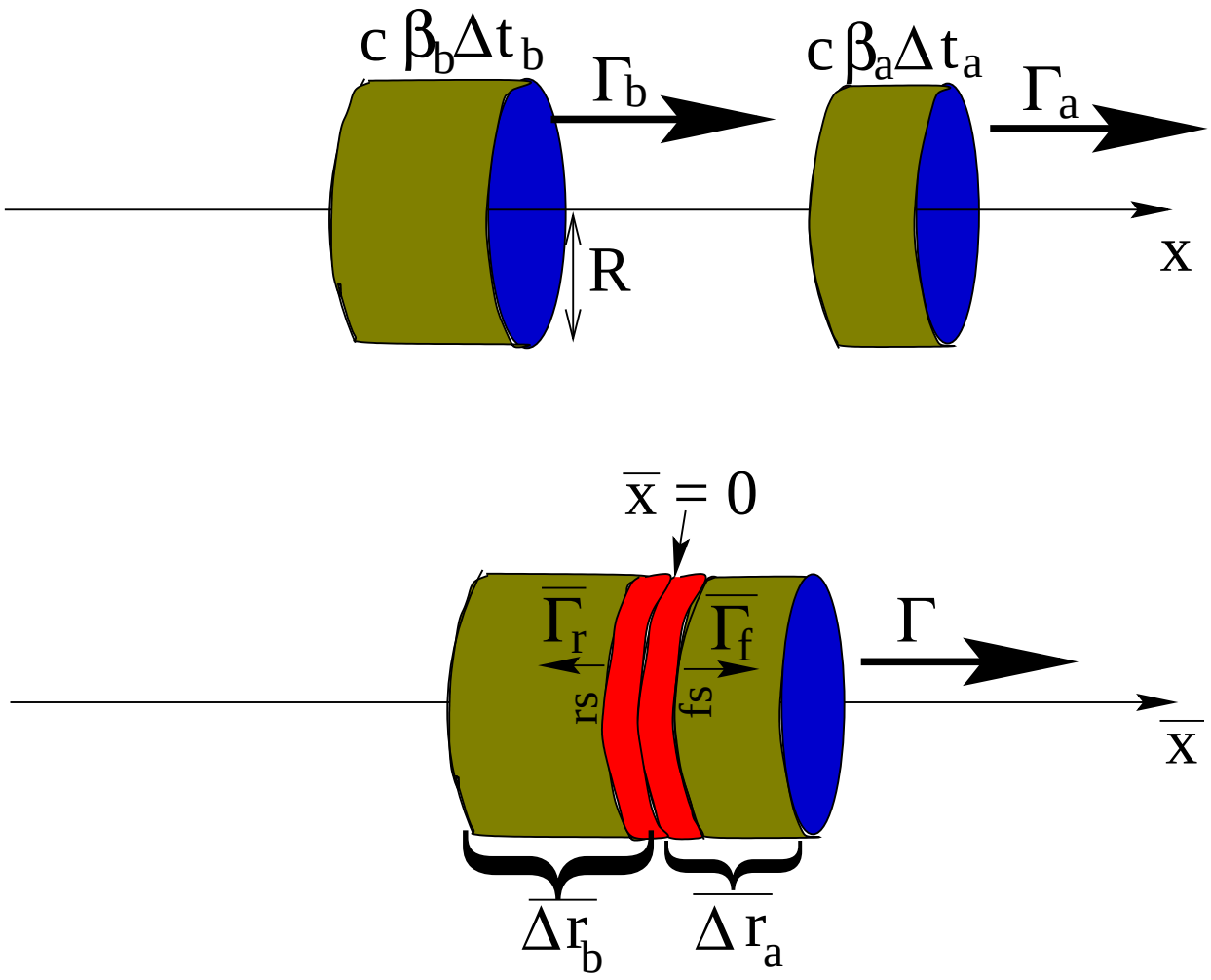


Fig. 1.— Schematic of the colliding-shell geometry.

The collision between the two shells will lead to the formation of a forward shock moving into the slower shell a, and a reverse shock moving back into shell b. In the following, an overline denotes quantities in the frame of the shocked material behind the shock fronts. In this frame, the forward and reverse shocks move with Lorentz factors $\overline{\Gamma}_{f,r}$, respectively, away from the contact discontinuity. Pressure equilibrium across the contact discontinuity yields the condition

$$n'_a \left(\overline{\Gamma}_f^2 - \overline{\Gamma}_f\right) = n'_b \left(\overline{\Gamma}_r^2 - \overline{\Gamma}_r\right). \tag{2}$$

Denoting the bulk Lorentz factor of the shocked material with respect to the stationary (AGN) rest frame as Γ (with velocity βc), the shell velocities can be transformed to the

shocked fluid frame through

$$\overline{\Gamma}_{f,r} = \Gamma_{a,b}\Gamma\,(1 - \beta_{a,b}\,\beta). \tag{3}$$

Eqs. 2 and 3 can be solved to find Γ, $\overline{\Gamma_f}$ and $\overline{\Gamma_r}$. The solution is obtained numerically (cf. Sari & Piran 1995; Panaitescu & Mészáros 1999; Dermer 2008).

The widths of the shells in the shocked-fluid frame are given by

$$\overline{\Delta r}_{a,b} = \frac{\Gamma_{a,b}\,c\,\Delta t_{a,b}}{\overline{\Gamma}_{f,r}} \tag{4}$$

where we have set $\beta_{a,b} = 1$ since $\Gamma_{a,b} \gg 1$. The time it takes for the shocks to cross their respective shells, can then be calculated as

$$\overline{\Delta t}_{f,r} = \frac{\Gamma_{a,b}\,\Delta t_{a,b}}{\overline{\Gamma}_{f,r}\,\overline{\beta}_{f,r}} \tag{5}$$

in the shocked-fluid frame.

3. Relativistic Particle Dynamics

Relativistic particles are entering the shocked-fluid region with collective Lorentz factors $\overline{\Gamma}_{f,r}$, respectively. Upon shock crossing, the plasma will be compressed by a compression ratio r. For the results presented in §5, we have used $r = 4$. We assume that a fraction ϵ_B of the energy density in the shocked plasma will be contained in the magnetic field behind the shock fronts, which yields

$$B_{f,r} = \sqrt{8\pi r\,\epsilon_B\,\left(\overline{\Gamma}^2_{f,r} - \overline{\Gamma}_{f,r}\right) n'_{a,b}\,m_p c^2} \tag{6}$$

for the magnetic field strength behind the shocks.

First- and second-order Fermi processes will accelerate particles at the shock fronts. We characterize the resulting injection of relativistic particles into the shocked-fluid frame through the parameter ϵ_e giving the fraction of the shocked plasma kinetic energy in the shocked-fluid frame that is transferred into relativistic electrons. Thus the injection power in relativistic electrons at the shock fronts is given by

$$\left.\frac{dE_{f,r}}{dt}\right|_{\rm rel.e} = \epsilon_e\,\pi R^2\,m_p c^3\,n'_{a,b}\,\overline{\Gamma}_{f,r}\overline{\beta}_{f,r}\,\left(\overline{\Gamma}_{f,r} - 1\right). \tag{7}$$

The injection of relativistic electrons is described as a power-law in electron energy, $E_e = \gamma m_e c^2$,

$$\frac{dn_e}{d\gamma\,dt} \equiv Q(\gamma) = Q_0\,\gamma^{-q}\,H(\gamma;\gamma_1,\gamma_2) \tag{8}$$

where the triple-argument Heaviside function is defined as $H(x;a,b)=1$ if $a\le x\le b$ and 0 otherwise, and all γ's refer to the shocked-fluid frame. We parameterize the width of the acceleration zone within the shocked-fluid region as a multiple $\Delta_{\rm acc}$ of the Larmor radius of a proton with $\gamma_p=\overline{\Gamma}_{f,r}$ in the shocked-fluid frame,

$$\overline{\Delta r}_{\rm acc;f,r}=\Delta_{\rm acc}\,\frac{\overline{\Gamma}_{f,r}\,m_pc^2}{e\,B_{f,r}}\sim 3\times10^6\,\Delta_{\rm acc}\,\left(\frac{B_{f,r}}{\rm G}\right)^{-1}\,\overline{\Gamma}_{f,r}\ {\rm cm}. \tag{9}$$

Consequently, the particle injection at any given point in the shocked-fluid region will be active for a time

$$\overline{\Delta t}_{\rm acc;f,r}=\Delta_{\rm acc}\,\frac{\overline{\Gamma}_{f,r}\,m_pc}{e\,B_{f,r}\,\overline{\beta}_{f,r}}\sim 10^{-4}\,\Delta_{\rm acc}\,\left(\frac{B_{f,r}}{\rm G}\right)^{-1}\,\overline{\Gamma}_{f,r}\,\overline{\beta}_{f,r}^{-1}\ {\rm s}. \tag{10}$$

Particle acceleration will hence be active in a volume $\overline{V}_{\rm acc;f,r}=\pi R^2\,\overline{\Delta r}_{\rm acc;f,r}$. This allows us to evaluate the normalization of the particle injection function (8) as

$$Q_{0;f,r}=\frac{\epsilon_e\,\pi R^2\,m_pc\,n'_{a,b}\,\overline{\Gamma}_{f,r}\overline{\beta}_{f,r}\,\left(\overline{\Gamma}_{f,r}-1\right)}{\overline{V}_{\rm acc;f,r}\,m_e}\times\begin{cases}\frac{q-2}{\gamma_1^{2-q}-\gamma_2^{2-q}} & \text{if } (q\neq2)\\ \frac{1}{\ln\left(\frac{\gamma_2}{\gamma_1}\right)} & \text{if } q=2.\end{cases} \tag{11}$$

The high-energy cutoff can be obtained by balancing the acceleration time scale of electrons with the synchrotron loss time scale. Writing the acceleration time scale as a factor $a_{\rm acc}$ times the electron gyration time scale, $t_{\rm acc}=2\pi\,a_{\rm acc}\,\gamma\,m_ec^2/(e\,B)$, the maximum electron Lorentz factor will be given by

$$\gamma_{2;f,r}=\sqrt{\frac{3\,e}{a_{\rm acc}\,\sigma_T\,B_{f,r}}}\approx 4.6\times10^7\,a_{\rm acc}^{-1/2}\,\left(\frac{B_{f,r}}{\rm G}\right)^{-1/2} \tag{12}$$

If a fraction ζ_e of electrons behind the shock fronts is accelerated into the power-law distribution (8) and we assume $\gamma_2\gg\gamma_1$, then the low-energy cutoff of the injection function (8) is given by

$$\gamma_{1;f,r}=\begin{cases}\frac{m_p}{m_e}\,\frac{q-2}{q-1}\,\frac{\epsilon_e}{\zeta_e}\,(\overline{\Gamma}_{f,r}-1) & \text{if } q>2\\ \left(\frac{m_p}{m_e}\,\frac{2-q}{q-1}\,\frac{\epsilon_e}{\zeta_e}\,[\overline{\Gamma}_{f,r}-1]\,\gamma_{2;f,r}^{q-2}\right)^{\frac{1}{q-1}} & \text{if } 1<q<2\\ \frac{m_p}{m_e}\,\frac{\epsilon_e}{\zeta_e}\,(\overline{\Gamma}_{f,r}-1)/\ln\left(\frac{\gamma_{2;f,r}}{\gamma_{1;f,r}}\right) & \text{if } q=2\end{cases}$$

(13)

where the $q = 2$ case will be solved numerically.

The electrons injected according to Eq. 8 will subsequently cool primarily due to radiative losses. Adiabatic losses become important after the shocks have traversed the shell and the shocked fluid shell begins to expand. When this happens, the magnetic field and therefore the synchrotron emission rapidly decays (Dermer 2008). We neglect adiabatic losses in this study because of the rapid radiative cooling of the electrons. A good approximation to the time-dependent shape of the electron distribution can be found if all radiative losses can be described by a loss term

$$\dot{\gamma} = -\nu_0 \gamma^2 \tag{14}$$

which holds for synchrotron emission in a constant magnetic field as well as Compton scattering in the Thomson regime in a radiation field of constant energy density. In that case,

$$\nu_0 = \frac{4}{3}\, c\, \sigma_T\, \frac{u}{m_e c^2} \tag{15}$$

where u is the sum of the magnetic-field and radiation field energy densities in the shocked-fluid frame. If the system under consideration is (a) SSC dominated and/or (b) Compton scattering at any given electron energy is predominantly happening in the Klein-Nishina regime, the evolution of the electron distribution can only be solved numerically. This is because in case (a), the dominant radiation field for Compton cooling depends on the current (and recent) electron energy distribution and thus the cooling becomes non-linear (see, e.g., Röken & Schlickeiser 2009; Schlickeiser 2009, for an analytical treatment of non-linear radiative cooling), and in case (b), the cooling curve flattens towards higher energies compared to the simple γ^2 dependence in Eq. 14. Therefore, our analysis is most directly applicable to the FSRQs and LBLs in which the γ-ray emission is generally believed to be dominated by EC scattering, mostly in the Thomson regime.

If the conditions of a constant energy density u and Compton scattering in the Thomson regime are approximately fulfilled, then the time-dependent electron distribution can be found analytically. For this purpose, we define a spatial coordinate $\overline{x}$ which is defined in the shocked-fluid frame as $\overline{x} = 0$ at the contact discontinuity, and is measured positive in the direction of the forward-shock propagation (i.e., into shell a; see Fig. 1). At any given point $\overline{x}$, the time $\overline{t}_x$ elapsed since the onset of the acceleration (i.e., since the forward or reverse shock has passed this point), is given by

$$\overline{t}_x = \overline{t} - \frac{|\overline{x}|}{\overline{\beta}_{f,r}\, c} \tag{16}$$

where $\overline{t}$ denotes the reference time in the shocked-fluid frame. At any given point, the acceleration will remain active for a time $\overline{\Delta t}_{\rm acc;f,r}$. Then, the time- and space-dependent relativistic, non-thermal electron distribution can be well approximated by

$$\overline{n}(\gamma;\overline{x},\overline{t}_x) = Q_0\, H(\overline{t}_x)\, H(\gamma_{\rm up}-\gamma) \left\{ \min(\overline{t}_x, \overline{\Delta t}_{\rm acc;f,r})\, \gamma^{-q}\, H(\gamma;\gamma_1,\gamma_c) \right.$$
$$\left. + \frac{\min(\overline{t}_x, \overline{\Delta t}_{\rm acc;f,r})}{\nu_0\, \overline{t}_x}\, \gamma^{-(1+q)}\, H(\gamma-\gamma_1)\, H(\gamma;\gamma_c,\gamma_{\rm up}) \;+\; \overline{\Delta t}_{\rm acc;f,r}\, \gamma_1^{-q}\, \gamma^{-2} H(\gamma;\gamma_{\rm min},\gamma_1) \right\} \tag{17}$$

where the single-argument Heaviside function is defined as $H(x) = 1$ if $x > 0$ and 0 otherwise, and the characteristic electron energies are given by

$$\begin{aligned} \gamma_{\rm up} &= \frac{1}{\gamma_2^{-1} + \nu_0\, \max\{0, (\overline{t}_x - \overline{\Delta t}_{\rm acc;f,r})\}} \\ \gamma_c &= \frac{1}{\nu_0 \overline{t}_x}, \\ \gamma_{\rm min} &= \frac{1}{\gamma_1^{-1} + \nu_0 \overline{t}_x}. \end{aligned} \tag{18}$$

4. Radiative Output

The evaluation of the radiative output from the entire shock structure will involve an integral of the emissivity $j_{\overline{\epsilon}}$ along the $\overline{x}$ direction:

$$\nu F_\nu(\epsilon, t_{\rm obs}) = \frac{D^4\, \pi R^2}{d_L^2} \int_{\overline{x}_{\rm min}}^{\overline{x}_{\rm max}} \overline{\epsilon}\, j_{\overline{\epsilon}}(\overline{x}, \overline{t}_{\rm x,em})\, d\overline{x} \tag{19}$$

where $D = (\Gamma\,[1-\beta\mu])^{-1}$ is the Doppler boosting factor with $\mu = cos\theta$, the cosine of the viewing angle between the jet axis and the line of sight, and $\overline{\epsilon} = \epsilon\,(1+z)/D$. The emission time $\overline{t}_{\rm x,em}$ has to be evaluated accounting for the light-travel time difference between different parts of the jet. The integration at a given observer's time $t_{\rm obs}$ has to be performed in a way that $dt_{\rm obs} = (1+z)\,(dt - dx\,\mu/c) = 0$, where t and x are measured in the stationary AGN frame. With $d\overline{t} = dt/\Gamma$ and $d\overline{x} = \Gamma dx$, we find that an advancement in $d\overline{x}$ corresponds to

an advancement in emission time as $d\overline{t} = d\overline{x}\,\mu/(\Gamma^2 c)$. Consequently, the co-moving emission time elapsed since the shock-crossing at any given point $\overline{x}$ at observed time corresponding to co-moving time $\overline{t}$ will be

$$\overline{t}_{\rm x,em} = \overline{t} - \frac{|\overline{x}|}{\overline{\beta}_{f,r} c} + \frac{\overline{x}\,\mu}{\Gamma^2 c}. \tag{20}$$

The limits $\overline{x}_{\rm min,max}$ of the integration in Eq. 19 will be given by constraints on the emission time being > 0 (i.e., the shock front must have passed the point $\overline{x}$), and the thickness of the shell:

$$\begin{aligned} \overline{x}_{\rm min} &= -\min\left(\frac{\overline{t}\,\overline{\beta}_r\,c}{1+\mu\overline{\beta}_r/\Gamma^2}\,,\,\overline{\Delta r}_b\right) \\ \overline{x}_{\rm max} &= \min\left(\frac{\overline{t}\,\overline{\beta}_f\,c}{1-\mu\overline{\beta}_f/\Gamma^2}\,,\,\overline{\Delta r}_a\right) \end{aligned} \tag{21}$$

There will be the additional constraint of particles being available to contribute to the emission at a given energy $\overline{\epsilon}$, which depends on the individual emission mechanisms considered below.

4.1. Synchrotron Emission

For the purpose of our analytical treatment, we use a simple δ-function approximation for the synchrotron emissivity:

$$j_{\overline{\epsilon},\rm sy} = \frac{c\,\sigma_T\,B^2\,\overline{\epsilon}}{48\pi^2\,b^2\,\gamma_{\rm sy}}\,n_e(\gamma_{\rm sy}) \tag{22}$$

where $b = B/B_{\rm crit}$ with $B_{\rm crit} = (m_e c^3)/(e\hbar) \approx 4.4\times10^{13}$ G, and $\gamma_{\rm sy} = \sqrt{\overline{\epsilon}/b}$. Inserting this into Eq. 19 yields

$$\nu F_\nu^{\rm sy}(\epsilon, t_{\rm obs}) = \frac{D^{5/2}}{\sqrt{1+z}}\,\frac{c\,\sigma_T\,B^2\,R^2}{48\,\pi\,d_L^2\,b^{3/2}}\,\epsilon^{3/2}\int_{\overline{x}_{\rm min}}^{\overline{x}_{\rm max}} n_e\left(\sqrt{\frac{\epsilon\,(1+z)}{b\,D}}\,,\,\overline{t}_{\rm x,em}\right)\,d\overline{x} \tag{23}$$

where we use Eq. 17 for the space- and time-dependent particle distribution $n_e(\gamma_{\rm sy}, \overline{t}_{\rm x,em})$. The integral in 23 can be solved fully analytically, and the solution is derived in Appendix A.

In this study, we focus on predictions for optical and higher-frequency emission. For this reason, we neglect synchrotron-self absorption (SSA) in our analysis. The emission region of our model system becomes optically thick to SSA at frequencies well below the optical regime. In our model systems considered in §5, the SSA frequency (where $\tau_{\rm SSA} = 1$) is typically $\lesssim \nu_{\rm SSA} \sim 10^{13}$ Hz.

4.2. External-Compton Emission

For the purpose of an analytical treatment, we evaluate the Comptonization of external radiation also with a simple δ-function approximation for the Thomson cross section. Furthermore, we assume that the external radiation field is isotropic in the stationary AGN frame and characterize it as mono-energetic with frequency $\nu_{\rm ext}$, corresponding to a dimensionless photon energy in the co-moving frame, $\overline{\epsilon}_s = \Gamma\, h\nu_{\rm ext}/(m_e c^2)$. The radiation energy density $u_{\rm ext}$ in the stationary AGN frame will be boosted into the shocked-fluid frame as $\overline{u}_{\rm ext} = \Gamma^2 u_{\rm ext}$. The effect of the Klein-Nishina decline of the Compton cross section is approximated as a hard cutoff in the scattered photon spectrum at $\epsilon_c = (D/[1+z]\,\overline{\epsilon}_s)$. The beaming patterns of the intrinsically isotropic synchrotron and the external-Compton emissions are slightly different because the external radiation field is anisotropic in the co-moving frame (Dermer 1995). However, as long as the observer is located within the beaming cone at $\theta_{\rm obs} \sim 1/\Gamma$, the difference is small and will be neglected in our simplified semi-analytical treatment. With these approximations, the treatment of the external Compton radiation is completely analogous to the one of synchrotron emission (see Appendix A), with the substitutions $B^2/(8\pi) \to \overline{u}_{\rm rad}$ and $b \to \overline{\epsilon}_s$:

$$\nu F_\nu^{\rm EC}(\epsilon, t_{\rm obs}) = \frac{D^{5/2}}{\sqrt{1+z}}\,\frac{c\,\sigma_T\,\overline{u}_{\rm rad}\,R^2}{6\,d_L^2\,\overline{\epsilon}_s^{3/2}}\,\epsilon^{3/2}\,H\left(\frac{D}{(1+z)\,\overline{\epsilon}_s} - \epsilon\right)\int_{\overline{x}_{\rm min}}^{\overline{x}_{\rm max}} n_e\left(\sqrt{\frac{\epsilon\,(1+z)}{\overline{\epsilon}_s\,D}}\,,\,\overline{t}_{\rm x,em}\right)\,d\overline{x} \tag{24}$$

with the solution to the integral given by the sum of the terms $I_{ir} + I_{if}$ $(i = 1, 2, 3)$ for $\gamma = \sqrt{(\epsilon\,(1+z)/[\overline{\epsilon}_s\,D])}$ derived in Appendix A.

4.3. Synchrotron Self-Compton Emission

For the evaluation of the synchrotron-self-Compton emissivity $j_{\overline{\epsilon},\rm SSC}$, to use in Eq. 19, we adopt, again, a δ-function approximation for the Compton cross section,

$$\frac{d\sigma}{d\epsilon_c\, d\Omega_c} \approx \sigma_T\, \delta(\epsilon_c - \gamma^2[1-\beta\overline{\mu}_c]\epsilon_s)\, \delta(\Omega_c - \Omega_e)\; H(1-\gamma\epsilon_s[1-\beta\overline{\mu}_c]). \tag{25}$$

where $\overline{\mu}_c$ is the cosine of the collision angle between the scattering electron and the incoming soft photon with energy ϵ_s. In Eq. 25 the effect of the Klein-Nishina decline of the Compton cross section is incorporated as a hard cutoff at the transition from the Thomson to the Klein-Nishina regime. With these approximations, the Compton emissivity becomes

$$j_{\overline{\epsilon},\mathrm{SSC}}(\overline{x},\overline{t}_{\mathrm{x,em}}) \approx \frac{c\,\sigma_T\, m_e c^2}{8\pi}\overline{\epsilon}^{1/2} \int\limits_{4\pi} d\overline{\Omega}_s \int\limits_{0}^{1/(\overline{\epsilon}[1-\overline{\mu}_c])} d\overline{\epsilon}_s\, \sqrt{1-\overline{\mu}_c}\, \frac{\overline{n}_{\mathrm{ph}}(\overline{\epsilon}_s,\overline{\Omega}_s,\overline{x},\overline{t}_{\mathrm{x,em}})}{\overline{\epsilon}_s^{1/2}}\, n_e(\gamma_c,\overline{x},\overline{t}_{x,em}) \tag{26}$$

with

$$\gamma_c = \sqrt{\frac{\overline{\epsilon}}{(1-\beta\overline{\mu}_c)\,\overline{\epsilon}_s}} \tag{27}$$

For relativistic electrons, $\gamma \gg 1$ we can neglect the factor β in Eq. 27 as long as $\overline{\mu}_c \ll \beta \sim 1$, so that it is an explicit solution. In order to use Eq. 26, we need an expression for the synchrotron photon density $\overline{n}_{\mathrm{ph}}(\overline{\epsilon}_s,\overline{\Omega}_s)$, which is a convolution of the (retarded) contributions from all shocked parts of the jet. For simplicity, we assume that all synchrotron photons enter a given point along the jet either directly from the front (superscript '+') or from the back (superscript '-'). In those cases, the scattering angle $\overline{\mu}_c$ is determined through the angular δ distribution in Eq. 25 as

$$\overline{\mu}_c^{\pm} = \mp\overline{\mu} = \mp\frac{\mu-\beta_\Gamma}{1-\beta_\Gamma\mu} \tag{28}$$

where μ is the cosine of the observing angle in the observer's frame and $\beta_\Gamma = \sqrt{1-1/\Gamma^2}$. We then write the synchrotron photon density as

$$\overline{n}_{\mathrm{ph}}(\overline{\epsilon}_s,\overline{\Omega}_s,\overline{x},\overline{t}_{\mathrm{x,em}}) \equiv \overline{n}^{+}_{\mathrm{ph}}(\overline{\epsilon}_s,\overline{x},\overline{t}_{\mathrm{x,em}})\frac{\delta(\mu_c+\overline{\mu})}{2\pi} + \overline{n}^{-}_{\mathrm{ph}}(\overline{\epsilon}_s,\overline{x},\overline{t}_{\mathrm{x,em}})\frac{\delta(\mu_c-\overline{\mu})}{2\pi} \tag{29}$$

where now the evaluation of $\overline{n}^{\pm}_{\mathrm{ph}}(\overline{\epsilon}_s)$ involves an integral over the retarded emission from the shocked parts of the jet in front of and behind the point under consideration, respectively. This is requires the evaluation of an integral

$$\overline{n}^{\pm}_{\rm ph}(\overline{x}) = \frac{1}{4\pi\, c} \int\limits_{\overline{x}^{\pm}_{\rm s,min}}^{\overline{x}^{\pm}_{\rm s,max}} d\overline{x}'\, \dot{n}_{\rm ph}(\overline{x}') \int\limits_{0}^{R} \frac{r\, dr}{([\overline{x}-\overline{x}']^2 + r^2)}$$

$$= \frac{1}{8\pi\, c} \int\limits_{\overline{x}^{\pm}_{\rm s,min}}^{\overline{x}^{\pm}_{\rm s,max}} d\overline{x}'\, \dot{n}_{\rm ph}(\overline{x}') \ln\left(\frac{(\overline{x}-\overline{x}')^2 + R^2}{(\overline{x}-\overline{x}')^2}\right) \tag{30}$$

The physically relevant case at hand here will correspond to thin slabs with $R \gg \overline{\Delta r}_{\rm a,b}$, for which the integral simplifies to

$$\overline{n}^{\pm}_{\rm ph}(\overline{x}) = \frac{1}{4\pi\, c} \int\limits_{\overline{x}^{\pm}_{\rm s,min}}^{\overline{x}^{\pm}_{\rm s,max}} d\overline{x}'\, \dot{n}_{\rm ph}(\overline{x}')\, \ln\left(\frac{R}{|\overline{x}-\overline{x}'|}\right) \tag{31}$$

The photon density distributions $\overline{n}^{\pm}_{\rm ph}$ are evaluated fully analytically, as discussed in Appendix B, while the remaining two integrations over $\overline{\epsilon}_s$ and $\overline{x}$ will be done numerically. Those are the only numerical integrations needed in our evaluation of the time-dependent emission spectra and light curves from the internal shock model.

In our analysis, we neglect second-order SSC emission. This is justified by (a) the small Thomson depth ($\sim 10^{-4}$) of our model systems considered in the following section, and (b) the Klein-Nishina suppression of higher-order SSC emission.

5. Results

We have applied the semi-analytical internal-shock model described in the previous section, to parameter sets typical for FSRQs and LBLs. In these objects, the γ-ray emission is generally believed to be dominated by Compton scattering of external photons in the Thomson regime, in which case our approximate description of a constant electron cooling coefficient ν_0 is valid. Table 1 lists parameters which we adopt for a baseline model in this regime. The chosen model parameters result in a bulk Lorentz factor of the shocked fluid of $\Gamma = 18.2$, and a relative Lorentz factor between the shells of $\Gamma_{\rm rel} = 1.133$. The observing angle $\theta_{\rm obs}$ has been chosen to coincide with the angle for which $D = \Gamma$, and we take the ϵ_e and ϵ_B parameters equal in the forward and reverse shocked regions.

Fig. 2 shows the instantaneous broadband spectra from this baseline model. In order to compare the SEDs with observations typically requiring extended exposure times, we also

evaluate the average SED over an integration time of 30 ksec. This time is representative of a deep blazar observation in X-rays, though shorter than typically required for Fermi to accumulate a signal with useful photon statistics from a bright γ-ray blazar. For Fermi, the minimum observation time from signal-dominated statistics for the detection of $5N_5$ photons at 1 GeV photon energy is $t_{obs} \gtrsim 25N_5/(X_{1/5} \cdot 8000 \text{ cm}^2 \cdot 10^{-10} f_{-10} \text{ erg cm}^{-2} \text{ s}^{-1} \cdot 1.6 \times 10^{-3} \text{ ergs/GeV}) \approx 5 \times 10^4 N_5/(X_{1/5} f_{-10})$ s, where $0.2\, X_{1/5}$ is the fraction of time that Fermi will effectively observe any given target in scanning mode covering about 2.4 sr (Atwood et al. 2009). For the bright flare parameters used in Fig. 2, the νF_ν flux at 1 GeV reaches values of $\approx 5 \times 10^{13}$ Jy Hz or $f_{-10} \sim 5$, so that variability as short as ≈ 3 hours could be detected. For comparison, the brightest blazar flare yet detected with Fermi was from 3C 454.3, which reached flux levels $\gtrsim 2{\times}10^{-5}$ ph (> 100 MeV) cm^{-2} s^{-1} (Escande & Tanaka 2009), somewhat dimmer than the example considered here.

The time-averaged SED is illustrated by the heavy solid curve in Fig. 2. It displays a synchrotron peak in the infrared, at $\sim 2 \times 10^{13}$ Hz ($\lambda \sim 15\mu$m), as well as an EC dominated γ-ray peak at $\sim 10^{22}$ Hz (~ 40 MeV), with the γ-ray flux dominating over the synchrotron peak flux. It also displays a very hard, SSC-dominated X-ray spectrum ($\alpha_X < 1$). These SED properties are representative of blazars of the FSRQ subclass, e.g., PKS 1510-089 (D'Ammando et al. 2009) or 3C 454.3 (Abdo et al. 2009b). We note that due to the hard low-energy cutoff introduced by our delta function approximation to the Compton emissivity, the emission in the hard X-ray – soft γ-ray ($\sim$ 100 keV – a few MeV) region may be underproduced in our simulations.

The snap-shot SEDs in Fig. 2 illustrate that the high-energy end of the synchrotron peak, emitted directly behind the forward and reverse shock fronts, remains essentially unaffected as long as the observer receives synchrotron emission from the shocks still being located within the shells. As the shocks propagate, an increasingly larger region of the shells is energized with particles having longer time to cool. Therefore, the synchrotron spectrum extends to progressively lower frequencies. As the observer sees the shock regions leaving the shells, the highest-energy electrons rapidly cool off, leading to a loss of the high-frequency synchrotron emission. In the SSC component, the light-travel time delay leads to a delayed response of the SSC emission with respect to the synchrotron emission, with slightly cooled electrons still being able to efficiently Thomson scatter synchrotron photons up to γ-ray energies.

Fig. 3 shows the light curves in the optical (R-band), X-rays (1 keV), and high-energy (HE) γ-rays in the Fermi range (100 MeV and 1 GeV) resulting from our baseline model simulation. The synchrotron-dominated optical and the EC-dominated HE γ-ray light curves exhibit similar shapes, dominated by a rapid onset of the emission, a continued gradual

build-up as long as the shocks are located within the shells, and a rapid decay dominated by radiative cooling. The time scale of this decay is inversely proportional to the characteristic electron energy responsible for the respective emission. This explains the more rapid decay of the 1 GeV light curve compared to the 100 MeV one. The X-ray light curve, dominated by SSC emission, exhibits a much more gradual decay due to the broad-band convolution of electron and synchrotron photon energies involved to produce emission at any given frequency. At $\sim 1.6 \times 10^4$ s, the optical emission begins to be dominated by low-frequency SSC emission characterized by a slow, gradual decay.

We point out that generally, blazars exhibit a low intensity of quiescent emission throughout the electromagnetic spectrum, which will prevent the observed light curves to reach the very low emission levels predicted for the beginning and very late times of our simulation. Assuming that this quiescent level of emission exhibits only moderate variability, it will lead to more moderate variability amplitudes, but will not affect the conclusions about cross correlations and time lags presented in the following.

Even though some features of the SEDs and light curves in Figures 2 and 3 are artifacts of our simplified analytical treatment of the time- and space-dependent particle distributions and the radiation processes, our results are expected to capture the salient spectral and light curve features as they would result from a more detailed numerical treatment. In particular, comparison is to be made with cross-correlation and time lag features that can realistically be extracted from unevenly sampled observational data. This is routinely done using the DCF of Edelson & Krolik (1988). Thefore, for direct comparison with observational results, we apply the same formalism to our simulated light curves. The DCFs between the optical, X-ray and 100 MeV light curves shown in Figure 3, are plotted in Figure 4.

Figure 4 illustrates that the more gradual decay of the (SSC-dominated) X-ray light curve with respect to the optical one translates into an optical lead before the X-rays by about 2 hr. The 100 MeV (EC) emission is produced by electrons of lower energy than the R-band optical synchrotron emission. This leads to a more gradual light curve decay at 100 MeV, translating into a γ-ray lag of $\sim$ 1 hr behind the optical, and a reduced lag of X-rays behind the 100 MeV γ-rays (compared to the X-ray – optical lag) by only about $\sim$ 1 hr. All bands show a strong correlation with a DCF peak > 0.9.

The characteristics of the injected electron distribution are evaluated according to Eqs. (13) and (12). In our baseline model, these are $\gamma_{1,f} = 130$, $\gamma_{1,r} = 350$, and $\gamma_{2;f,r} = 4.6 \times 10^4$. The magnetic field, according to Eq. 6 is 1.0 G in both shocked regions. We note that the inferred values of γ_1 are substantially higher than the characteristic values of $\gamma_1 \sim$ a few inferred by Ghisellini et al. (2009) and Sikora et al. (2009). In principle, similar values could also be achieved with different parameter choices in our simulations. However, in order to

still produce a synchrotron peak in the same range as observed in FSRQs, a substantially higher magnetic field ($B \gtrsim 10$ G) would be required. Therefore, if the model explored here is applicable to FSRQs and LBLs with parameters close to the ones chosen in our parameter study, one would infer a substantially smaller total number of nonthermal electrons and hence a smaller total jet power than found in Ghisellini et al. (2009) and Sikora et al. (2009).

Starting from our baseline model discussed above, we are now investigating the influence of the various parameters listed in Table 1 on the SED and light curve features. For each set of parameters, we evaluate the time-averaged SED over an integration time of 30 ksec to find the location of the synchrotron and Compton peaks as well as the Compton dominance, defined as $CD = \nu F_\nu^{\rm IC}/\nu F_\nu^{\rm sy}$. For each simulation, we calculate the DCFs between the optical (R-band), X-ray (1 keV), and HE γ-ray (100 MeV) light curves, and find the predicted time delay and peak value of the DCF.

Specifically, we explore variations of the following parameters and their influence on the resulting time-averaged SED, inter-band time lags and DCF peaks:

- The external radiation energy density, $u_{\rm ext}$
- The electron equipartition fraction, ϵ_e
- The magnetic-field equipartition fraction, ϵ_B
- The fraction of electrons accelerated, ζ_e
- The electron acceleration time scale parameter, $a_{\rm acc}$
- The electron injection spectral index, q
- The time scales of relativistic shell ejection, $\Delta t_{\rm a,b}$
- The relative Lorentz factors of the colliding shells, $\Gamma_{\rm rel} \approx (1/2)(\Gamma_a/\Gamma_b + \Gamma_b/\Gamma_a)$
- The kinetic power of the faster shell, L_b
- The radius of the shells, R

Each parameter is varied individually, leaving all other parameters constant at the value of our baseline model (Table 1). In the following, we discuss the influence of each individual parameter mentioned above, on the SED and DCF characteristics.

5.1. Variations of $u_{\rm ext}$

An increasing external radiation energy density leads to a transition from SSC to EC dominated γ-ray production and overall more rapid electron cooling. The consequences in the SED are decreasing synchrotron and EC peak frequencies, along with a decreasing synchrotron peak flux and an increasing Compton peak flux (see Fig. 5). This shift in SED characteristics (Fossati et al. 1998) reflects the gradual transition from BL-Lacs to FSRQs along the blazar sequence as suggested by Ghisellini et al. (1998). The dependence of the external field energy density shown in Fig. 5 would only apply to the FSRQs and LBLs, which have peak synchrotron frequencies between 10^{13} and 10^{14} Hz. In order to extend this to XBLs and the blazar sequence, it may also be necessary to posit a correlation between jet power and the external broad-line region density (Böttcher & Dermer 2002; Ghisellini & Tavecchio 2008).

Fig. 6 illustrates the dependence of time lags and DCF peak values on the external radiation energy density. For high values of $u_{\rm ext}$ ($\gtrsim 3 \times 10^{-4}$ erg cm^{-3}), the more rapid cooling with incresing $u_{\rm ext}$ leads to generally decreasing time lags. For smaller values of $u_{\rm ext}$, we begin to see the effects of SSC emission becoming significant in the γ-ray regime. Most notably, this ultimately leads to an inversion of the optical – HE γ-ray lead into a lag of optical behind HE γ-rays for very low $u_{\rm ext}$. The reason for this is that the SSC γ-rays at 100 MeV are produced by electrons of higher energy than those emitting synchrotron radiation in the R band.

All three bands remain generally well correlated (DCF peak $\gtrsim 0.75$), with only a weak trend towards lower correlation quality for SSC dominated high-energy emission.

5.2. Variations of ϵ_e

With increasing electron equipartition fraction ϵ_e, the total energy input into relativistic electrons increases, along with an increase in the low-energy cutoff of the injected electron distribution. The increased electron energy density leads to an increasing radiative output in both spectral components (synchrotron and Compton) as well as an increasing fraction of SSC to synchrotron emission. Since the HE γ-ray emission remains EC dominated for our parameters, the Compton dominance remains essentially unchanged. The peak frequencies of the two spectral components remain essentially unchanged for realistic values of $\epsilon_e \lesssim 0.1$ (see Figure 7).

There is an overall weak trend of decreasing inter-band time lags with increasing ϵ_e, which is related to decreasing electron cooling time scales. All three bands remain well

correlated (DCF peak $\gtrsim 0.85$) irrespective of ϵ_e.

5.3. Variations of ϵ_B

The parameter ϵ_B regulates the magnetic field. An increasing value of ϵ_B implies stronger synchrotron cooling. In the synchrotron frequency range, this effect is largely cancelled out by the increase in the characteristic synchrotron frequency ($\nu_{\rm sy} \propto \gamma^2\, B$). Therefore, the synchrotron peak frequency remains essentially unchanged as ϵ_B changes, while the Compton peak frequency decreases (see Fig. 9).

As a consequence of the limited amount of power available to channel into synchrotron and Compton emission, the Compton peak flux remains almost constant with varying ϵ_B, while the synchrotron peak flux continuously increases, consequently leading to a decreasing Compton dominance.

In the DCFs (see Figure 10), there is a general trend of decreasing time lags and increasing quality of correlations with increasing ϵ_B. This is a consequence of the decreasing radiative cooling time scales (with progressively larger contributions from synchrotron and SSC cooling).

5.4. Variations of ζ_e

Increasing the fraction ζ_e of electrons accelerated, while keeping the power injected into relativistic electron (parametrized by ϵ_e) constant, leads to a decreasing low-energy cutoff of the electron distribution. As ζ_e increases, an increasing fraction of the available power in electrons will be distributed at low electron energies, leading to a decreasing radiative output. Consequently, both the synchrotron and Compton peak frequencies as well as the synchrotron and Compton peak fluxes decrease with increasing ζ_e.

Less efficient radiative cooling because of lower average particle energies leads to a gradual trend of increasing time lags with increasing ζ_e.

5.5. Variations of $a_{\rm acc}$

The electron acceleration efficiency parameter $a_{\rm acc}$ regulates the high-energy cutoff of the injected electron population via Eq. 12. A lower value of $a_{\rm acc}$ implies a larger value of γ_2. Changes in $a_{\rm acc}$ (and hence γ_2) have a negligible influence on the location of the

sychrotron and Compton peaks, both in frequency and flux (for electron spectral indices $q > 2$). However, the value of $a_{\rm acc}$ (and hence, γ_2) determines whether the synchrotron emission of freshly injected electrons extends into the X-ray regime or cuts off at optical-UV frequencies. As $a_{\rm acc}$ increases, the synchrotron emission cuts off at progressively lower frequencies. Specifically, this leads to an increasingly rapid decline of the R-band emission after the shocks have broken out of the shells. As long as the synchrotron emission of freshly emitted electrons does extend beyond the R-band, this leads to an increasing R-band lead before the X-ray emission. For a very high value of $a_{\rm acc}$ (10^8 in our simulations), even the synchrotron emission of freshly injected electrons cuts off at frequencies close the R-band, and the R-band flux is dominated by low-frequency SSC emission very early on. This reverses the R-band vs. X-ray lead into a lag. A similar argument applies to the dependence of the 100 MeV γ-ray emission with respect to X-rays and optical.

All light curves correlate well with DCF peakds $\gtrsim 0.9$, with no substantial dependence on $a_{\rm acc}$.

5.6. Variations of q

The electron spectral index at the time of injection, q, obviously directly determines the spectral shape of the synchrotron and Compton emissions. In particular, for hard injection spectra ($q \lesssim 2$), the peak frequencies are determined primarily by the energy of the highest-energy electrons. As we choose a steeper injection electron spectrum, the peak shifts to a position where it is predominantly determined by the low-energy cut-off γ_1 and thus only weakly dependent on the electron injection index (see Figure 12).

Generally, a harder electron injection spectrum (lower q) implies that a larger fraction of the energy transferred to electrons is stored in high-energy electrons. This leads to a monotonic increase of the Compton dominance with decreasing q (harder electron spectrum).

Generally, all frequency bands correlate well with DCF peak values $\gtrsim 0.8$. There is a slight trend of de-correlation of the HE γ-rays with optical and X-rays for hard injection spectra ($q \lesssim 2.3$). The increasing quality of correlation with softening injection spectra goes in tandem with decreasing absolute values of the time lags. Notably, for very steep injection spectra ($q \geq 3$), the instantaneous synchrotron emission in the R band has a very steep spectral index so that a substantial fraction of the R-band flux is contributed by very-low-frequency SSC emission. This reverses the R-band lead observed for harder injection spectra into an R-band lag behind X-rays and HE γ-rays.

5.7. Variations of $\Delta t_{\rm a,b}$

The shell ejection time scale determines the width of the shells. This in turn, regulates the shock propagation time and thereby the dynamical time scale of the shocked emission region. Furthermore, since we left the ejection power constant, a longer ejection time corresponds to a larger total kinetic energy deposited into the shells. This latter effect causes the overall radiative power output to increase with $\Delta t_{\rm a,b}$. The Compton peak is dominated by EC, so that the Compton dominance remains essentially unchanged. The values of the peak frequencies show only a weak increasing trend with increasing $\Delta t_{\rm a,b}$.

The most notable trend in the DCF features is a reversal of the lag of R behind HE γ-rays (100 MeV) into a lead for long shock propagation time scales, in tandem with an increasing X-ray lag behind HE γ-rays. This is due to the fact that both X-rays and R-band are dominated, at least at late times, by slowly decaying SSC emission. As the shocked regions are more extended, SSC emission persists for a longer time due to light-travel time delays pertinent to the SSC emission. In contrast, the decay of the EC-dominated HE γ-ray emission is determined only by the radiative cooling time scale, which is independent of $\Delta t_{\rm a,b}$ with the assumptions made here. It is notable that the time lags are generally not proportional to the dynamical time of the shock propagation, as one could naively expect.

5.8. Variations of $\Gamma_{\rm rel}$

We have explored the effect of an increasing difference in the Lorentz factors of the colliding shells, leading to an increasing relative Lorentz factor, $\Gamma_{\rm rel} \approx (1/2)\,(\Gamma_a/\Gamma_b + \Gamma_b/\Gamma_a)$, by varying Γ_a and Γ_b in a way that the resulting shocked-fluid Lorentz factor Γ (and hence the Doppler boosting factor D) remains unchanged. An increase in $\Gamma_{\rm rel}$ drastically increases the radiative efficiency of the shells. The increased energy density in the shocked shells will, at the same time, increase the magnetic fields and decrease the radiative cooling time scales. It will also lead to larger shock propagation Lorentz factors $\overline{\Gamma}_{f,r}$ and hence larger low-energy cut-offs in the electron distributions. This leads to a net increase of the peak frequencies of both radiation components with increasing $\Gamma_{\rm rel}$. The peak fluxes in both components increase drastically with increasing $\Gamma_{\rm rel}$ with only a moderate effect on the Compton dominance. The decreasing radiative cooling time scales with increasing $\Gamma_{\rm rel}$ imposes a general trend of shortening inter-band time lags with only minor effect on the DCF peak values (see Fig. 15).

5.9. Variations of L_b

Varying the kinetic luminosity of one of the shells, keeping its Lorentz factor unchanged, directly amounts to increasing its particle density. For unchanged ϵ_B, this will also increase the magnetic field. Both effects lead to an increasing synchrotron peak flux and a decreasing Compton dominance. Due to more rapid radiative (synchrotron) cooling, both peak peak frequencies decrease with increasing L_b. As the system becomes increasingly synchrotron + SSC dominated, the light-travel time delays inherent to SSC emission lead to a general trend of increasing time delays with increasing L_b, accompanied by very moderate changes in the DCF peak values.

5.10. Variations of R

Increasing the shell radius implies a smaller particle density and hence a lower magnetic field. Consequently, the synchrotron peak flux and peak frequency decrease with increasing shell radius, leading to an increasing Compton dominance.

In the DCFs, an increasing radius R leads to a gradually increasing trend of time lags between R and higher-frequency bands with slightly decreasing DCF peak values ($\sim 0.95 \rightarrow 0.8$ for $R = 3 \times 10^{15}$ cm $\rightarrow$ 3×10^{16} cm). The increasing time lag trend may be related to the increasing synchrotron cooling time as R increases.

6. Summary and Conclusions

We have developed a semi-analytical internal-shock model for blazars. Our model includes synchrotron, SSC, and external Compton emission, and properly takes into account light-travel time and shock-propagation effects as well as the space- and time-dependent relativistic electron distributions in the shocked shell region to evaluate the time-dependent radiative output. For direct comparison with sparsely and unevenly sampled observational data, we evaluated the Discrete Correlation Functions between several representative wavelengths, namely between the optical R band, 1 keV X-rays, and high-energy γ-rays (100 MeV — Fermi).

Our calculations were used to characterize inter-band time lags and the quality of the correlation, as represented by the peak value of the DCF. For this calcuation, we considered a specific model blazar where spectral variability could be detected with optical and pointing X-ray telescopes at the derived flux level. These calculations can be extended to apply to

brighter blazars where variability might be detected with the Fermi telescope, or otherwise used to model the time-averaged SED observed with Fermi. Keeping these caveats in mind, we have studied the influence of variations of a number of essential model parameters on the resulting SED and DCF characteristics.

We note that our model results apply to FSRQs and LBLs, maybe IBLs, but not HBLs, because of the restriction to the Thomson regime. The parameter choices in our model are extensive, including ϵ_e and ϵ_B parameters, shell widths, collision radii, and jet powers. We have reduced the allowed parameter space by taking equal shell powers, with the forward and reverse shocks having equal ϵ_e and ϵ_B parameters. By examining the dependence of peak frequency, peak νF_ν flux and Compton dominance in Fig. 5, we find a trend in accord with the behavior of the blazar sequence (Fossati et al. 1998).

Our results do not directly explain the break in the νF_ν spectra at a few GeV in blazars like 3C 454.3 and AO 0235+164 and other FSRQs and LBLs (Abdo et al. 2009a,b), or the relative constancy of the GeV spectral index with flux state. The GeV breaks in several blazar SEDs can not be explained as a cooling break since, whenever photon statistics allow a reliable determination of the break, it is $\Delta\alpha > 0.5$. However, a smooth high-energy cutoff could effectively mimic a spectral break, and such a cutoff around a few GeV could be produced in our model by a lower high-energy cutoff of the electron distribution, which could be achieved with a choice of a larger value for our paramter $a_{\rm acc}$.

We have not considered a detailed spectral comparison with the impressive multiwavelength SEDs now available due to campaigns involving the Fermi Gamma Ray Space Telescope (Abdo et al. 2009c). Rather, here we considered a parameter study of short timescale variability between optical, X-ray, and gamma-ray eneriges.

In most cases, the optical light curves showed substantial leads (by $\sim$ a few hours) before X-ray and HE γ-ray emission. However, variations of several parameters (e.g., the external radiation energy density $u_{\rm ext}$, the acceleration time scale parameter $a_{\rm acc}$, the electron spectral index q, and the shell widths) can drastically change the amount and even sign of the time delays. This may explain the lack of a consistent pattern of inter-band time lags when comparing multiple observing epochs of the same object (e.g., Hartman et al. 2001).

MB acknowledges partial support from NASA through INTEGRAL Guest Investigator grant NNX09AI71G and Fermi Guest Investigator grant NNX09AT82G. The work of CDD is supported by the Office of Naval Research.

REFERENCES

Abdo, A. A., et al. 2009, ApJ, 700, 597

Abdo, A. A., et al. 2009, ApJ, 699, 817

Abdo, A. A., et al. 2009, ApJ, 697, 934

Aharonian, F., et al., 2007b, ApJ, 664, L71

Albert, J., et al., 2007, ApJ, 669, 862

Atwood, W. B., et al. 2009, ApJ, 697, 1071

Blażejowski, M., et al., 2005, ApJ, 630, 130

Böttcher, M., & Chiang, J., 2002, ApJ, 581, 127

Böttcher, M., & Dermer, C. D. 2002, ApJ, 564, 86

Böttcher, M., 2007a, in proc. "The Multimessenger Approach to Gamma-Ray Sources", ApSS, 309, 95

Böttcher, M., et al., 2007, ApJ, 670, 968

Chiaberge, M., & Ghisellini, G., 1999, MNRAS, 306, 551

Costamante, L., 2008, IJMP D, 17, 1449

D'Ammando, F., et al., 2009, A&A, in press (arXiv:0909.3484)

Dermer, C. D., 1995, ApJ, 446, L63

Dermer, C. D. 1998, ApJ, 501, L157

Dermer, C. D. 2008, ApJ, 684, 430

Edelson, R. A., & Krolik, J. H., 1988, ApJ, 333, 646

Escande, L., & Tanaka, Y. T., 2009, Astronomer's Telegram # 2328, 1

Fossati, G., et al., 2000, ApJ, 541, 166

Fossati, G., Maraschi, L., Celotti, A., Comastri, A., & Ghisellini, G. 1998, MNRAS, 299, 433

Georganopoulos, M., & Marscher, A. P., 1998, ApJ, 506, 621

Ghisellini, G., Celotti, A., Fossati, G., Maraschi, L., & Comastri, A., 1998, MNRAS, 301, 451

Ghisellini, G., Tavecchio, F., & Ghirlanda, G. 2009, MNRAS, 399, 2041

Ghisellini, G., & Tavecchio, F. 2008, MNRAS, 387, 1669

Graff, P. B., Georganopoulos, M., Perlman, E. S., & Kazanas, D., 2008, 689, 68

Hartman, R. C., et al., 2001, ApJ, 558, 583

Horan, D., et al., 2009, ApJ, 695, 596

Joshi, M., & Böttcher, M., 2007, ApJ, 662, 884

Joshi, M., 2009, Ph.D. Thesis, Ohio University

Kataoka, J., et al., 2000, ApJ, 528, 243

Kirk, J. G., Rieger, F. M., & Mastichiadis, A., 1998, A&A, 333, 452

Krawczynski, H., et al., 2004, ApJ, 601, 151

Kusunose, M., Takahara, F., & Li, H., 2000, ApJ, 536, 299

Li, H., & Kusunose, M., 2000, ApJ, 536, 729

MAGIC Collaboration, et al. 2008, Science, 320, 1752

Meszaros, P., Laguna, P., & Rees, M. J. 1993, ApJ, 415, 181

Mimica, P., Aloy, M. A., Müller, E., & Brinkmann, W., 2004, A&A, 418, 947

Mücke, A., & Protheroe, R. J., 2001, Astropart. Phys., 15, 121

Mücke, A., et al., 2003, Astropart. Phys., 18, 593

Panaitescu, A., & Mészáros, P. 1999, ApJ, 526, 707

Röken, C., & Schlickeiser, R., 2009, A&A, 503, 309

Sari, R., Piran, T., & Halpern, J. P. 1999, ApJ, 519, L17

Sari, R., & Piran, T. 1995, ApJ, 455, L143

Schlickeiser, R., 2009, MNRAS, 398, 1483

Sikora, M., Stawarz, Ł., Moderski, R., Nalewajko, K., & Madejski, G. M. 2009, ApJ, 704, 38

Sokolov, A., Marscher, A. P., & McHardy, I. A., 2004, ApJ, 613, 725

Spada, M., Ghisellini, G., Lazzati, D., & Celotti, A., 2001, MNRAS, 325, 1559

Takahashi, T., et al., 1996, ApJ, 470, L89

Zhang, Y. H., et al., 2002, ApJ, 572, 762

A. Time-dependent Synchrotron Spectra

Since the particle energy distribution of Eq. 17 explicitly depends on $\overline{t}_{\rm em}$, it is convenient to transform the integration (23) into an integration over emission time, using

$$d\overline{t}_{\rm em} = \left(\frac{\mu}{\Gamma^2 c} - \frac{{\rm sign}(\overline{x})}{\overline{\beta}_{f,r}\, c} \right) d\overline{x}. \tag{A1}$$

As mentioned above, the limits $\overline{x}_{\rm min,max}$ of Eq. 21 will then be augmented by the condition that $n(\gamma_{\rm sy}, \overline{t}_{\rm em}) > 0$ for a given electron energy $\gamma_{\rm sy}$. Since $\mu/\Gamma^2 < 1/\overline{\beta}_{f,r}$ in the parameter range relevant to internal shocks in blazars ($\mu \sim 1$; $\Gamma >> 1$, $\overline{\beta}_{f,r} \sim 1$), the emission times will be $\leq \overline{t} = t_{\rm obs}(1+z)/D$ throughout the integration region. Thus, defining a time limit $\overline{t}_f$ corresponding to the limit $x_{\rm max}$ in the forward shock region and $\overline{t}_r$ corresponding to $x_{\rm min}$ in the reverse shock region, the integral in Eq. 23 will consist of two branches,

$$\int\limits_{\overline{x}_{\rm min}}^{\overline{x}_{\rm max}} n_e \left(\sqrt{\frac{\epsilon\,(1+z)}{b\,D}}\,,\, \overline{t}_{\rm x,em} \right) d\overline{x} = \left\{ \int\limits_{\overline{t}_f}^{\overline{t}} \frac{d\overline{t}_{\rm x,em}}{\frac{1}{\overline{\beta}_f\, c} - \frac{\mu}{\Gamma^2 c}} + \int\limits_{\overline{t}_r}^{\overline{t}} \frac{d\overline{t}_{\rm x,em}}{\frac{\mu}{\Gamma^2 c} + \frac{1}{\overline{\beta}_r\, c}} \right\} n_e \left(\sqrt{\frac{\epsilon\,(1+z)}{b\,D}}\,,\, \overline{t}_{\rm x,em} \right) \tag{A2}$$

The limits on $\overline{x}$ in Eq. 21 can then be converted into limits on $\overline{t}_{\rm x,em}$ as

$$\overline{t}_r \quad = \quad \max \left\{ 0\,,\, \left(\min \left[\frac{\overline{t}\,\overline{\beta}_r\, c}{1 + \frac{\mu \overline{\beta}_r}{\Gamma^2}}\,,\, \overline{\Delta r}_b \right] \left[\frac{\mu}{\Gamma^2 c} + \frac{1}{\overline{\beta}_r\, c} \right] \right) \right\}$$

This preprint was prepared with the AAS LaTeX macros v5.2.

$$\overline{t}_f \quad = \quad \max\left\{0\ ,\ \left(\min\left[\frac{\overline{t}\,\overline{\beta}_f\,c}{1-\frac{\mu\,\overline{\beta}_f}{\Gamma^2}}\ ,\ \overline{\Delta r}_a\right]\left[\frac{\mu}{\Gamma^2 c}-\frac{1}{\overline{\beta}_f\,c}\right]\right)\right\} \tag{A3}$$

We now evaluate each term in the integral (A2) separately for each term in the expression for n in Eq. (17):

$$I_{1r} \equiv \frac{Q_0\,c\,\gamma^{-q}}{\left(\frac{\mu}{\Gamma^2}+\frac{1}{\overline{\beta}_r}\right)}\int_{\overline{t}_r}^{\overline{t}} H(\gamma_{\rm up}-\gamma)\,H(\gamma;\gamma_{1,r},\gamma_c)\,\min(\overline{t}_{\rm x,em},\overline{\Delta t}_{\rm acc,r})\,d\overline{t}_{\rm x,em}. \tag{A4}$$

This integral contributes only as long as

$$\begin{array}{rcll} \overline{t}_{\rm x,em} \geq & \overline{t}_r & & \text{(a)} \\ \overline{t}_{\rm x,em} \leq & \overline{t} & & \text{(b)} \\ \gamma \leq & \gamma_c = \frac{1}{\nu_0 \overline{t}_{\rm x,em}} & & \text{(c)} \\ \gamma \leq & \gamma_{\rm up} = \frac{1}{\gamma_{2,r}^{-1}+\nu_0\ \max(0,[\overline{t}_{\rm x,em}-\overline{\Delta t}_{\rm acc,r}])} & & \text{(d)} \end{array} \tag{A5}$$

These constraints translate into effective limits of the integral (A4) of

$$\begin{array}{rcl} \overline{t}_{\rm 1r,min} = & & \overline{t}_r \\ \overline{t}_{\rm 1r,max} = & \min\left\{\overline{t}\ ,\ \frac{1}{\nu_0\gamma}\ ,\ \left(\frac{1}{\nu_0}\left[\frac{1}{\gamma}-\frac{1}{\gamma_2}\right]+\overline{\Delta t}_{\rm acc,r}\right)\right\} & \end{array} \tag{A6}$$

and hence,

$$I_{1r} = \frac{Q_0\,c\,\gamma^{-q}}{\frac{\mu}{\Gamma^2}+\frac{1}{\overline{\beta}_r}}\,H(\gamma-\gamma_{1,\rm r})$$
$$\times\begin{cases} (1/2)(\overline{t}^2_{\rm 1r,max}-\overline{t}^2_{\rm 1r,min}) & \text{if } \overline{t}_{\rm 1r,min}<\overline{t}_{\rm 1r,max}<\overline{\Delta t}_{\rm acc,r} \\ (1/2)(\overline{\Delta t}^2_{\rm acc,r}-\overline{t}^2_{\rm 1r,min})+\overline{\Delta t}_{\rm acc,r}\,(\overline{t}_{\rm 1r,max}-\overline{\Delta t}_{\rm acc,r}) & \text{if } \overline{t}_{\rm 1r,min}\leq\overline{\Delta t}_{\rm acc,r}\leq\overline{t}_{\rm 1r,max} \\ \overline{\Delta t}_{\rm acc,r}\,(\overline{t}_{\rm 1r,max}-\overline{t}_{\rm 1r,min}) & \text{if } \overline{\Delta t}_{\rm acc,r}\leq\overline{t}_{\rm 1r,min}\leq\overline{t}_{\rm 1r,max} \end{cases} \tag{A7}$$

The forward-shock contribution of the first term is

$$I_{1f} \equiv \frac{Q_0\, c\, \gamma^{-q}}{\left(\frac{1}{\overline{\beta}_f} - \frac{\mu}{\Gamma^2}\right)} \int_{\overline{t}_f}^{\overline{t}} H(\gamma_{\rm up} - \gamma)\, H(\gamma; \gamma_{1,r}, \gamma_c)\, \min(\overline{t}_{\rm x,em}, \overline{\Delta t}_{\rm acc,r})\, d\overline{t}_{\rm x,em}. \tag{A8}$$

Analogous to the previous integral, the effective limits of this integration are

$$\begin{array}{rl} \overline{t}_{\rm 1f,min} = & \overline{t}_f \\ \overline{t}_{\rm 1f,max} = & \min\left\{\overline{t}\ ,\ \frac{1}{\nu_0 \gamma}\ ,\ \left(\frac{1}{\nu_0}\left[\frac{1}{\gamma} - \frac{1}{\gamma_2}\right] + \overline{\Delta t}_{\rm acc,f}\right)\right\} \end{array} \tag{A9}$$

and hence,

$$I_{1f} = \frac{Q_0\, c\, \gamma^{-q}}{\frac{1}{\overline{\beta}_f} - \frac{\mu}{\Gamma^2}}\, H(\gamma - \gamma_{1,\rm f})$$

$$\times \begin{cases} (1/2)(\overline{t}^2_{\rm 1f,max} - \overline{t}^2_{\rm 1f,min}) & \text{if } \overline{t}_{\rm 1f,min} < \overline{t}_{\rm 1f,max} < \overline{\Delta t}_{\rm acc,f} \\ (1/2)(\overline{\Delta t}^2_{\rm acc,f} - \overline{t}^2_{\rm 1f,min}) + \overline{\Delta t}_{\rm acc,f}\,(\overline{t}_{\rm 1f,max} - \overline{\Delta t}_{\rm acc,f}) & \text{if } \overline{t}_{\rm 1f,min} \le \overline{\Delta t}_{\rm acc,f} \le \overline{t}_{\rm 1f,max} \\ \overline{\Delta t}_{\rm acc,f}\,(\overline{t}_{\rm 1f,max} - \overline{t}_{\rm 1f,min}) & \text{if } \overline{\Delta t}_{\rm acc,f} \le \overline{t}_{\rm 1f,min} \le \overline{t}_{\rm 1f,max} \end{cases} \tag{A10}$$

The reverse-shock contribution from the second term in Eq. 17 is

$$I_{2\rm r} \equiv \frac{Q_0\, c\, \gamma^{-(q+1)}}{\left(\frac{\mu}{\Gamma^2} + \frac{1}{\overline{\beta}_r}\right)} \int_{\overline{t}_r}^{\overline{t}} H(\gamma; \gamma_c, \gamma_{\rm up})\, H(\gamma - \gamma_{1,\rm r})\, \frac{\min(\overline{t}_{\rm x,em}, \overline{\Delta t}_{\rm acc,r})}{\overline{t}_{\rm x,em}}\, d\overline{t}_{\rm x,em}. \tag{A11}$$

with the limits determined by the conditions

$$\begin{array}{rcll} \overline{t}_{\rm x,em} \ge & \overline{t}_r & & \text{(a)} \\ \overline{t}_{\rm x,em} \le & \overline{t} & & \text{(b)} \\ \gamma \ge & \gamma_c = \frac{1}{\nu_0 \overline{t}_{\rm x,em}} & & \text{(c)} \\ \gamma \le & \gamma_{\rm up} = \frac{1}{\gamma_{2,r}^{-1} + \nu_0\ \max(0, [\overline{t}_{\rm x,em} - \overline{\Delta t}_{\rm acc,r}])} & & \text{(d)} \end{array} \tag{A12}$$

These constraints translate into effective limits of the integral (A11) of

$$\begin{aligned} \overline{t}_{2\mathrm{r,min}} = & \quad \max\left\{\overline{t}_r \ , \ \tfrac{1}{\nu_0\,\gamma}\right\} \\ \overline{t}_{2\mathrm{r,max}} = & \quad \min\left\{\overline{t} \ , \ \left(\tfrac{1}{\nu_0}\ \left[\tfrac{1}{\gamma} - \tfrac{1}{\gamma_{2,r}}\right] + \overline{\Delta t}_{\mathrm{acc,r}}\right)\right\} \end{aligned} \tag{A13}$$

and hence,

$$I_{2\mathrm{r}} \equiv \frac{Q_0\, c\, \gamma^{-(q+1)}}{\left(\frac{\mu}{\Gamma^2} + \frac{1}{\overline{\beta}_r}\right)}\, H(\gamma - \gamma_{1,\mathrm{r}})$$

$$\times \begin{cases} \overline{t}_{2\mathrm{r,max}} - \overline{t}_{2\mathrm{r,min}} & \text{if } \overline{t}_{2\mathrm{r,min}} < \overline{t}_{2\mathrm{r,max}} < \overline{\Delta t}_{\mathrm{acc,r}} \\ \overline{\Delta t}_{\mathrm{acc,r}} - \overline{t}_{2\mathrm{r,min}} + \overline{\Delta t}_{\mathrm{acc,r}}\ \ln\left(\frac{\overline{t}_{2\mathrm{r,max}}}{\overline{\Delta t}_{\mathrm{acc,r}}}\right) & \text{if } \overline{t}_{2\mathrm{r,min}} \le \overline{\Delta t}_{\mathrm{acc,r}} \le \overline{t}_{2\mathrm{r,max}} \\ \overline{\Delta t}_{\mathrm{acc,r}}\ \ln\left(\frac{\overline{t}_{2\mathrm{r,max}}}{\overline{t}_{2\mathrm{r,min}}}\right) & \text{if } \overline{\Delta t}_{\mathrm{acc,r}} \le \overline{t}_{2\mathrm{r,min}} \le \overline{t}_{2\mathrm{r,max}} \end{cases} \tag{A14}$$

Analogously, for the forward-shock contribution from the second term in Eq. 17, we have the effective limits

$$\begin{aligned} \overline{t}_{2\mathrm{f,min}} = & \quad \max\left\{\overline{t}_f \ , \ \tfrac{1}{\nu_0\,\gamma}\right\} \\ \overline{t}_{2\mathrm{f,max}} = & \quad \min\left\{\overline{t} \ , \ \left(\tfrac{1}{\nu_0}\ \left[\tfrac{1}{\gamma} - \tfrac{1}{\gamma_{2,\mathrm{f}}}\right] + \overline{\Delta t}_{\mathrm{acc,f}}\right)\right\} \end{aligned} \tag{A15}$$

and hence,

$$I_{2\mathrm{f}} \equiv \frac{Q_0\, c\, \gamma^{-(q+1)}}{\left(\frac{1}{\overline{\beta}_f} - \frac{\mu}{\Gamma^2}\right)}\, H(\gamma - \gamma_{1,\mathrm{f}})$$

$$\times \begin{cases} \overline{t}_{2\mathrm{f,max}} - \overline{t}_{2\mathrm{f,min}} & \text{if } \overline{t}_{2\mathrm{f,min}} < \overline{t}_{2\mathrm{f,max}} < \overline{\Delta t}_{\mathrm{acc,f}} \\ \overline{\Delta t}_{\mathrm{acc,f}} - \overline{t}_{2\mathrm{f,min}} + \overline{\Delta t}_{\mathrm{acc,f}}\ \ln\left(\frac{\overline{t}_{2\mathrm{f,max}}}{\overline{\Delta t}_{\mathrm{acc,f}}}\right) & \text{if } \overline{t}_{2\mathrm{f,min}} \le \overline{\Delta t}_{\mathrm{acc,f}} \le \overline{t}_{2\mathrm{f,max}} \\ \overline{\Delta t}_{\mathrm{acc,f}}\ \ln\left(\frac{\overline{t}_{2\mathrm{f,max}}}{\overline{t}_{2\mathrm{f,min}}}\right) & \text{if } \overline{\Delta t}_{\mathrm{acc,f}} \le \overline{t}_{2\mathrm{f,min}} \le \overline{t}_{2\mathrm{f,max}} \end{cases} \tag{A16}$$

The third term in Eq. 17 yields a reverse-shock contribution of

$$I_{3\mathrm{r}} \equiv \frac{Q_0\, c\, \gamma^{-2}\, \gamma_{1,\mathrm{r}}^{(2-q)}}{\left(\frac{\mu}{\Gamma^2} + \frac{1}{\overline{\beta}_r}\right)} \int_{\overline{t}_r}^{\overline{t}} H(\gamma; \gamma_{\mathrm{min}}, \gamma_{1,\mathrm{r}})\ d\overline{t}_{\mathrm{x,em}}. \tag{A17}$$

with the limits determined by the conditions

$$\begin{array}{rcll} \overline{t}_{\rm x,em} \geq & \overline{t}_r & \quad {\rm (a)} \\ \overline{t}_{\rm x,em} \leq & \overline{t} & \quad {\rm (b)} \\ \gamma \geq & \gamma_{\rm min} = \frac{1}{\gamma_{\rm 1,r}^{-1} + \nu_0 \overline{t}_{\rm x,em}} & \quad {\rm (c)} \\ \gamma \leq & \gamma_{\rm max} & \quad {\rm (d)} \\ \gamma \leq & \gamma_{\rm 1,f} & \quad {\rm (e)} \end{array} \qquad (A18)$$

These constraints translate into effective limits of the integral (A17) of

$$\begin{array}{rl} \overline{t}_{\rm 3r,min} = & \max\left\{\overline{t}_r \ , \ \frac{1}{\nu_0}\left(\frac{1}{\gamma} - \frac{1}{\gamma_{\rm 1,r}}\right)\right\} \\ \overline{t}_{\rm 3r,max} = & \min\left\{\overline{t} \ , \ \left(\frac{1}{\nu_0}\left[\frac{1}{\gamma} - \frac{1}{\gamma_{2,r}}\right] + \overline{\Delta t}_{\rm acc,r}\right)\right\} \end{array} \qquad (A19)$$

and hence,

$$I_{\rm 3r} \equiv \frac{Q_0\, c\, \gamma^{-2}\, \gamma_{\rm 1,r}^{(2-q)}}{\left(\frac{\mu}{\Gamma^2} + \frac{1}{\overline{\beta}_r}\right)} \times (\overline{t}_{\rm 3r,max} - \overline{t}_{\rm 3r,min}) \qquad (A20)$$

Finally, the contribution of the third term in Eq. 17 from the forward shock is

$$I_{\rm 3f} \equiv \frac{Q_0\, c\, \gamma^{-2}\, \gamma_{\rm 1,r}^{(2-q)}}{\left(\frac{1}{\overline{\beta}_r} - \frac{\mu}{\Gamma^2}\right)} \times (\overline{t}_{\rm 3f,max} - \overline{t}_{\rm 3f,min}) \qquad (A21)$$

with the limits

$$\begin{array}{rl} \overline{t}_{\rm 3f,min} = & \max\left\{\overline{t}_f \ , \ \frac{1}{\nu_0}\left(\frac{1}{\gamma} - \frac{1}{\gamma_{\rm 1,f}}\right)\right\} \\ \overline{t}_{\rm 3f,max} = & \min\left\{\overline{t} \ , \ \left(\frac{1}{\nu_0}\left[\frac{1}{\gamma} - \frac{1}{\gamma_{2,f}}\right] + \overline{\Delta t}_{\rm acc,f}\right)\right\} \end{array} \qquad (A22)$$

B. Evaluation of the synchrotron photon density for SSC

For each incoming photon direction (±), the seed space- and time-dependent seed photon density $\overline{n}^{\pm}_{\rm ph}(\overline{\epsilon}_s\overline{x},\overline{t}_{\rm x,em})$ consists of contributions from all three branches of the electron distribution (17), and may contain contributions from both the forward and reverse shock. For any given branch of the electron distribution, the calculation is analogous for the various cases to be considered. Therefore, we give here only one representative case for each branch.

The space- and time-dependent photon density distribution is evaluated as

$$\overline{n}^{\pm}_{\rm ph}(\overline{\epsilon}_s,\overline{x},\overline{t}_{\rm x,em}) = \frac{\sigma_T}{48\pi^2\overline{\epsilon}_s^{1/2}\,m_e c^2}\int\limits_{\overline{x}^{\pm}_{\rm s,min}}^{\overline{x}^{\pm}_{\rm s,max}} \frac{B(\overline{x}')^2}{b(\overline{x}')^{3/2}}\,n_e\left(\sqrt{\frac{\overline{\epsilon}_s}{b(\overline{x}')}}\,,\,\overline{x}'\,,\,\overline{t}'_x\right)\,\ln\left(\frac{R}{|\overline{x}-\overline{x}'|}\right)\,d\overline{x}' \tag{B1}$$

where

$$\overline{t}'_x = \overline{t} - \frac{|\overline{x}'\,\mu|}{\overline{\beta}_{f,r}c} + \frac{\overline{x}}{\Gamma^2 c} - \frac{|\overline{x}'-\overline{x}|}{c}. \tag{B2}$$

Although $B(\overline{x}')$ and $b(\overline{x}')$ are constant throughout the forward shock region and the reverse shock region, we need to take into account that generally $B_f \neq B_r$. The integration limits in Eq. B1 are set by the conditions

$$\begin{array}{lccl} \overline{x}' \geq & \overline{x} & (\mathrm{a}^+) & \text{or} \\ \overline{x}' \leq & \overline{x} & (\mathrm{a}^-) & \\ \overline{t}'_x > & 0 & (\mathrm{b}) & \\ \overline{x}' \leq & \overline{\Delta r}_a & (\mathrm{c}) & \end{array} \tag{B3}$$

and hence

$$\begin{aligned} \overline{x}^{+}_{\rm s,min} &= \overline{x} \\ \overline{x}^{+}_{\rm s,max} &= \min\left\{\overline{\Delta r}_a\,,\,\left(\overline{\beta}_f\,\frac{c\overline{t}+\overline{x}\left[\frac{\mu}{\Gamma^2}+1\right]}{\overline{\beta}_f+1}\right)\right\} \end{aligned} \tag{B4}$$

$$\overline{x}^{-}_{\rm s,min} = -\min\left\{\overline{\Delta r}_b\,,\,\left(\overline{\beta}_r\,\frac{c\overline{t}+\overline{x}\left[\frac{\mu}{\Gamma^2}-1\right]}{\overline{\beta}_r+1}\right)\right\}$$

$$\overline{x}^{-}_{\rm x,max} = \qquad\qquad \overline{x} \tag{B5}$$

Because of the absolute values involved in $\overline{t}_x$ (Eq. B2), we need to evaluate the integral in Eq. B1 separately for the cases $\overline{x} > 0$ (A) and $\overline{x} < 0$ (B).

For case (A), the integral in Eq. B1 can be split up into 6 contributions:

$$I_s^{A\pm} \equiv \left(I_{s1}^{A\pm} + I_{s2}^{A\pm} + I_{s3}^{A\pm}\right) \tag{B6}$$

corresponding to the forward and backward traveling photons from the three terms in the expression for the electron density in Eq. 17. Hence,

$$I_{s1}^{A+} = Q_{0,f}\,\frac{B_f^2}{b_f^{3/2}}\gamma^{-q}\int_{\overline{x}^{+}_{\rm s,min}}^{\overline{x}^{+}_{\rm s,max}} H(\gamma_{\rm up}-\gamma)\,H(\gamma;\gamma_1,\gamma_c)\;\;\min\{\overline{t}_x, \overline{\Delta t}_{\rm acc,f}\}\,\ln\left(\frac{R}{|\overline{x}-\overline{x}'|}\right)\,d\overline{x}' \tag{B7}$$

with $\gamma = \sqrt{\overline{\epsilon}_s/b_f}$.

In the region corresponding to the A+ contribution, we parameterize the synchrotron emission time as

$$\overline{t}'_x \equiv \alpha_{\rm A+} - \beta_{\rm A+}\,\overline{x}' \tag{B8}$$

with

$$\begin{aligned} \alpha_{\rm A+} &= \;\; \overline{t} + \tfrac{\overline{x}}{c}\left(\tfrac{\mu}{\Gamma^2}+1\right) \\ \beta_{\rm A+} &= \qquad \tfrac{\overline{\beta}_f+1}{\overline{\beta}_f c} \end{aligned} \tag{B9}$$

The effective limits of the integration (B7) are determined by the Heaviside functions as

$$\begin{aligned} \overline{x}^{A+}_{\rm s1,min} &= \;\; \max\left\{\overline{x}^{+}_{\rm s,min}\,,\; \tfrac{1}{\beta_{A+}}\left(\alpha_{A+} - \tfrac{1}{\nu_{0,\rm f}\,\gamma} + \max\{0\,,\; [\nu_{0,\rm f}\,\gamma_2]^{-1} - \overline{\Delta t}_{\rm acc,f}\}\right)\right\} \\ \overline{x}^{A+}_{\rm s1,max} &= \qquad\qquad\qquad\qquad \overline{x}^{+}_{\rm s,max} \end{aligned} \tag{B10}$$

To evaluate the integral I_{s1}^{A+} with these limits, we define a critical $\overline{x}'_c$ for which $\overline{t}_x(\overline{x}'_c) = \overline{\Delta t}_{\rm acc,f}$:

$$\overline{x}'_{\rm c,A+} \equiv \frac{\alpha_{A+} - \overline{\Delta t}_{\rm acc,f}}{\beta_{A+}} \tag{B11}$$

with $\bar{t}_x < \overline{\Delta t}_{\rm acc,f}$ if $\overline{x}' > \overline{x}'_{\rm c,A+}$. Furthermore, we write

Then, the integration yields:

$$I_{s1}^{A+} = \gamma^{-q}\, Q_{0,f}\, \frac{B_f^2}{b_f^{3/2}}\, H(\gamma - \gamma_{1,\rm f}) \times$$

$$\begin{cases} R\, f_{s1}^{A+}(y)\Big|_{y_{\rm min}}^{y_{\rm max}} & \text{for } \overline{x}'_{\rm c,A+} < \overline{x}_{\rm s1,min}^{A+} < \overline{x}_{\rm s1,max}^{A+} \\ R\, f_{s1}^{A+}(y)\Big|_{y_c}^{y_{\rm max}} + \overline{\Delta t}_{\rm acc,f}\, R\, g(y)\Big|_{y_{\rm min}}^{y_c} & \text{for } \overline{x}_{\rm s1,min}^{A+} < \overline{x}'_{\rm c,A+} < \overline{x}_{\rm s1,max}^{A+} \\ \overline{\Delta t}_{\rm acc,f}\, R\, g(y)\Big|_{y_{\rm min}}^{y_{\rm max}} & \text{for } \overline{x}_{\rm s1,min}^{A+} < \overline{x}_{\rm s1,max}^{A+} < \overline{x}'_{\rm c,A+} \end{cases} \tag{B12}$$

with

$$\begin{aligned} y_{\rm min} &= \frac{\overline{x}_{\rm s1,min}^{A+} - \overline{x}}{R} \\ y_{\rm max} &= \frac{\overline{x}_{\rm s1,max}^{A+} - \overline{x}}{R} \\ y_c &= \frac{\overline{x}'_{\rm c,A+} - \overline{x}}{R} \end{aligned} \tag{B13}$$

and

$$\begin{aligned} f_{s1}^{A+}(y) &= (\beta_{A+}\, \overline{x} - \alpha_{A+})\, (y\, \ln y - y) + \tfrac{\beta_{A+}\, R\, y^2}{2}\, \left(\ln y - \tfrac{1}{2}\right) \\ g(y) &= y - y\, \ln y \end{aligned} \tag{B14}$$

Analogous calculations (carefully accounting for the different implications of the absolute values in Eq. B8 and the different magnetic-field values in the forward- and reverse-shock regions) yields the contributions A- and B± from the first term in Eq. 17.

The $A+$ ($\overline{x}' > \overline{x} > 0$) contribution of the second term in Eq. 17 is

$$I_{s2}^{A+} = Q_{0,f} \frac{B_f^2}{b_f^{3/2}}\, \gamma^{-(1+q)}\, H(\gamma - \gamma_{1,f}) \int_{\overline{x}_{\rm s,min}^{+}}^{\overline{x}_{\rm s,max}^{+}} \frac{H(\gamma; \gamma_c, \gamma_{\rm up})\, \min\{\overline{t}_x, \overline{\Delta t}_{\rm acc,f}\}}{\nu_{0,\rm f}\, \overline{t}_x}\, \ln\left(\frac{R}{\overline{x}' - \overline{x}}\right)\, d\overline{x}' \tag{B15}$$

The effective limits of this integration are

$$\begin{aligned} \overline{x}^{A+}_{\rm s2,min} = &\quad \max\left\{\overline{x}^{+}_{\rm s,min}\,,\,\tfrac{1}{\beta_{A+}}\left(\alpha_{A+}-\tfrac{1}{\nu_{0,\rm f}}\left[\tfrac{1}{\gamma}-\tfrac{1}{\gamma_{2,f}}\right]-\overline{\Delta t}_{\rm acc,f}\right)\right\} \\ \overline{x}^{A+}_{\rm s2,max} = &\quad \min\left\{\overline{x}^{+}_{\rm s,max}\,,\,\tfrac{1}{\beta_{A+}}\left(\alpha_{A+}-\tfrac{c}{\nu_{0,\rm f}\,\gamma}\right)\right\} \end{aligned} \tag{B16}$$

Using the parametrization for $\overline{t}_x$ from Eq. B8 and the critical value of $\overline{x}'$ from Eq. B11 for which $\overline{t}_x = \overline{\Delta t}_{\rm acc,f}$, the solution to I^{A+}_{S2} is

$$I^{A+}_{S2} = \frac{Q_{0,f}\,B_f^2}{\nu_{0,\rm f}\,b_f^{3/2}}\,\gamma^{-(1+q)}\,H(\gamma-\gamma_{1,f})\times$$

$$\begin{cases} \overline{\Delta t}_{\rm acc,f}\,f^{A+}_{s2}(y)\Big|_{y_{\rm min}}^{y_{\rm max}} & \text{for } \overline{x}^{A+}_{\rm s2,min} < \overline{x}^{A+}_{\rm s2,max} < \overline{x}'_{\rm c,A+} \\ \overline{\Delta t}_{\rm acc,f}\,f^{A+}_{s2}(y)\Big|_{y_{\rm min}}^{y_c} + R\,g(y)\Big|_{y_c}^{y_{\rm max}} & \text{for } \overline{x}^{A+}_{\rm s2,min} < \overline{x}'_{\rm c,A+} < \overline{x}^{A+}_{\rm s2,max} \\ R\,g(y)\Big|_{y_{\rm min}}^{y_{\rm max}} & \text{for } \overline{x}'_{\rm c,A+} < \overline{x}^{A+}_{\rm s2,min} < \overline{x}^{A+}_{\rm s2,max} \end{cases} \tag{B17}$$

with the definition of $y_{\rm min,max,c}$ analogous to Eq. B13, and

$$f^{A+}_{s2}(y) = \frac{\ln y\,\ln(\alpha_{A+}-\beta_{A+}\,[\overline{x}-R\,y])}{\beta_{A+}}$$

$$-\frac{1}{\beta_A}\left(\ln[\alpha_{A+}-\beta_{A+}\,\overline{x}]+\ln y-\frac{\beta_{A+}\,R\,y}{\alpha_{A+}-\beta_{A+}\,\overline{x}}\,\Phi\left[\frac{\beta_{A+}\,R\,y}{\alpha_{A+}-\beta_{A+}\,\overline{x}}\,,\,2\,,1\right]\right) \tag{B18}$$

where

$$\Phi(z,2,1) = \sum_{n=0}^{\infty}(n+1)^{-2}\,z^n \tag{B19}$$

is the Lerch function.

Again, analogous calculations yield the A- and B± contributions of the second term in Eq. 17.

The $A+$ ($\overline{x}' > \overline{x} > 0$) contribution of the third term in Eq. 17 is

$$I^{A+}_{s3} = \frac{Q_{0,f}\,B_f^2\,\overline{\Delta t}_{\rm acc,f}}{b_f^{3/2}}\,\gamma_{1,f}^{-q}\,\gamma^{-2}\int_{\overline{x}^{+}_{\rm s,min}}^{\overline{x}^{+}_{\rm s,max}} H(\gamma_{\rm up}-\gamma)\;H(\gamma;\gamma_{\rm min},\gamma_{1,f})\;\ln\left(\frac{R}{\overline{x}'-\overline{x}}\right)\,d\overline{x}' \tag{B20}$$

The effective integration limits are given by

$$\begin{aligned} \overline{x}^{A+}_{\rm s3,min} &= \max\left\{\overline{x}^{+}_{\rm s,min}\,,\ \frac{1}{\beta_{A+}}\,\left(\alpha_{A+}-\frac{1}{\nu_{0,\rm f}}\,\left[\frac{1}{\gamma}-\frac{1}{\gamma_{2,f}}\right]-\overline{\Delta t}_{\rm acc,f}\right)\right\} \\ \overline{x}^{A+}_{\rm s3,max} &= \min\left\{\overline{x}^{+}_{\rm s,max}\,,\ \frac{1}{\beta_{A+}}\,\left(\alpha_{A+}-\frac{1}{\nu_{0,\rm f}}\,\left[\frac{1}{\gamma}-\frac{1}{\gamma_{1,f}}\right]\right)\right\} \end{aligned} \qquad (B21)$$

and the result of the integration is then

$$I^{A+}_{s3} = \frac{Q_{0,f}\,B_f^2\,\overline{\Delta t}_{\rm acc,f}}{b_f^{3/2}}\,\gamma_{1,f}^{-q}\,\gamma^{-2}\,H(\gamma_{1,f}-\gamma)\,R\,\left(g[y_{\rm max}]-g[y_{\rm min}\right) \qquad \text{(B22)}$$

with

$$\begin{aligned} y_{\rm min} &= \frac{\overline{x}^{A+}_{\rm s3,min}-\overline{x}}{R} \\ y_{\rm max} &= \frac{\overline{x}^{A+}_{\rm s3,max}-\overline{x}}{R} \end{aligned} \qquad (B23)$$

Analogous solutions are obtained for the A- and B± contributions.

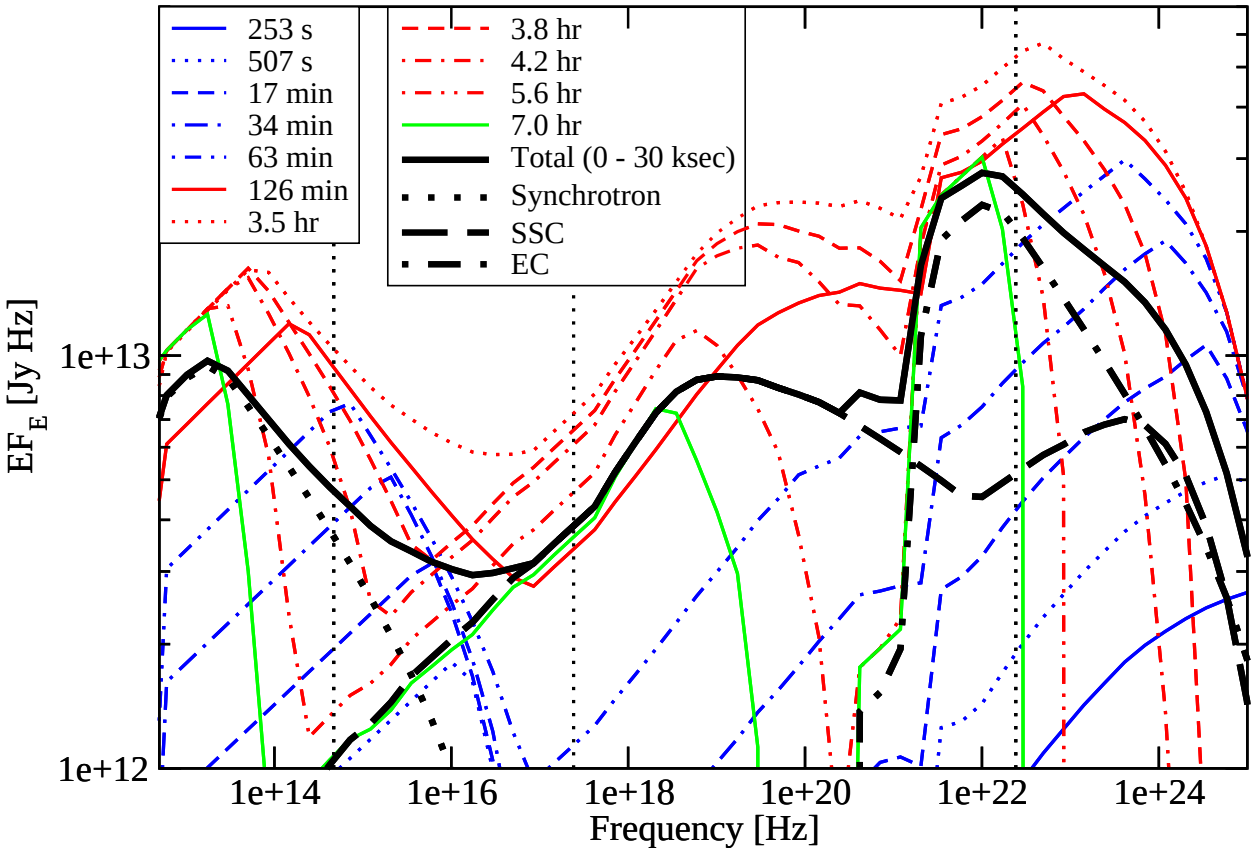


Fig. 2.— Snap-shot SEDs for our baseline model with parameters listed in Table 1. The heavy solid (red) curve shows the SED resulting from averaging over an integration time of 30 ksec, representative of a typical exposure time of a deep X-ray observation of a blazar. Individual radiation components of the time-averaged SED are shown as: dotted = synchrotron; long-dashed = SSC; dot-dashed = EC. The dotted vertical lines indicate the frequencies (R-band, 1 keV, 1 MeV, 100 MeV) at which light curves have been extracted.

Table 1. Parameters of our baseline model.

Parameter	Symbol	Value
Lorentz factor of shell a	Γ_a	15
Lorentz factor of shell b	Γ_b	25
Kinetic power of shell a	L_a	10^{49} erg s^{-1}
Kinetic power of shell b	L_b	10^{49} erg s^{-1}
Duration of ejection of shell a	Δt_a	2×10^3 s
Duration of ejection of shell b	Δt_b	2×10^3 s
Observing angle	$\theta_{\rm obs}$	3.15^o
Shell radius	R	3×10^{16} cm
Electron equipartition fraction	ϵ_e	0.1
B-field equipartition fraction	ϵ_B	10^{-3}
Electron acceleration fraction	ζ_e	0.01
Acceleration time scale par.	$a_{\rm acc}$	10^6
Acceleration length parameter	$\Delta_{\rm acc}$	10
Elect. injection spectral index	q	2.6

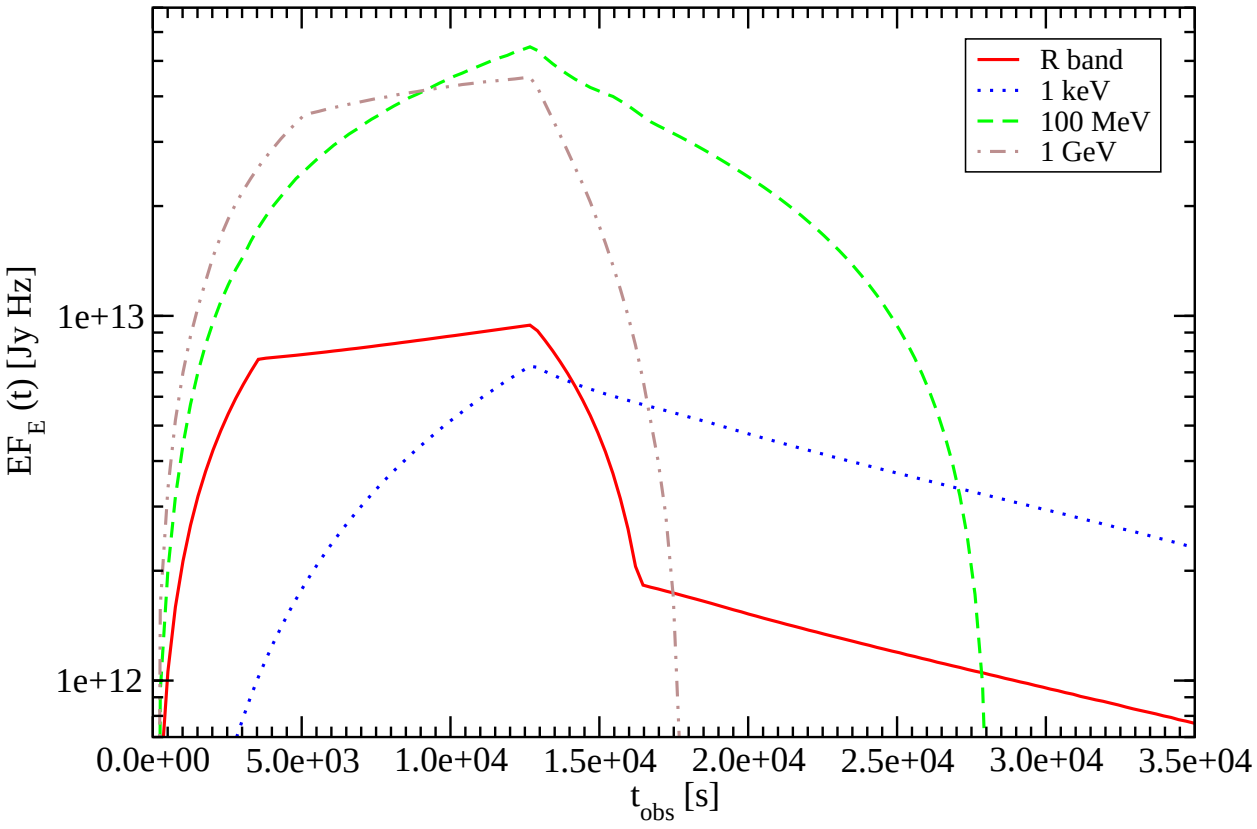


Fig. 3.— Light curves at various frequencies/energies resulting from our baseline model with parameters listed in Table 1.

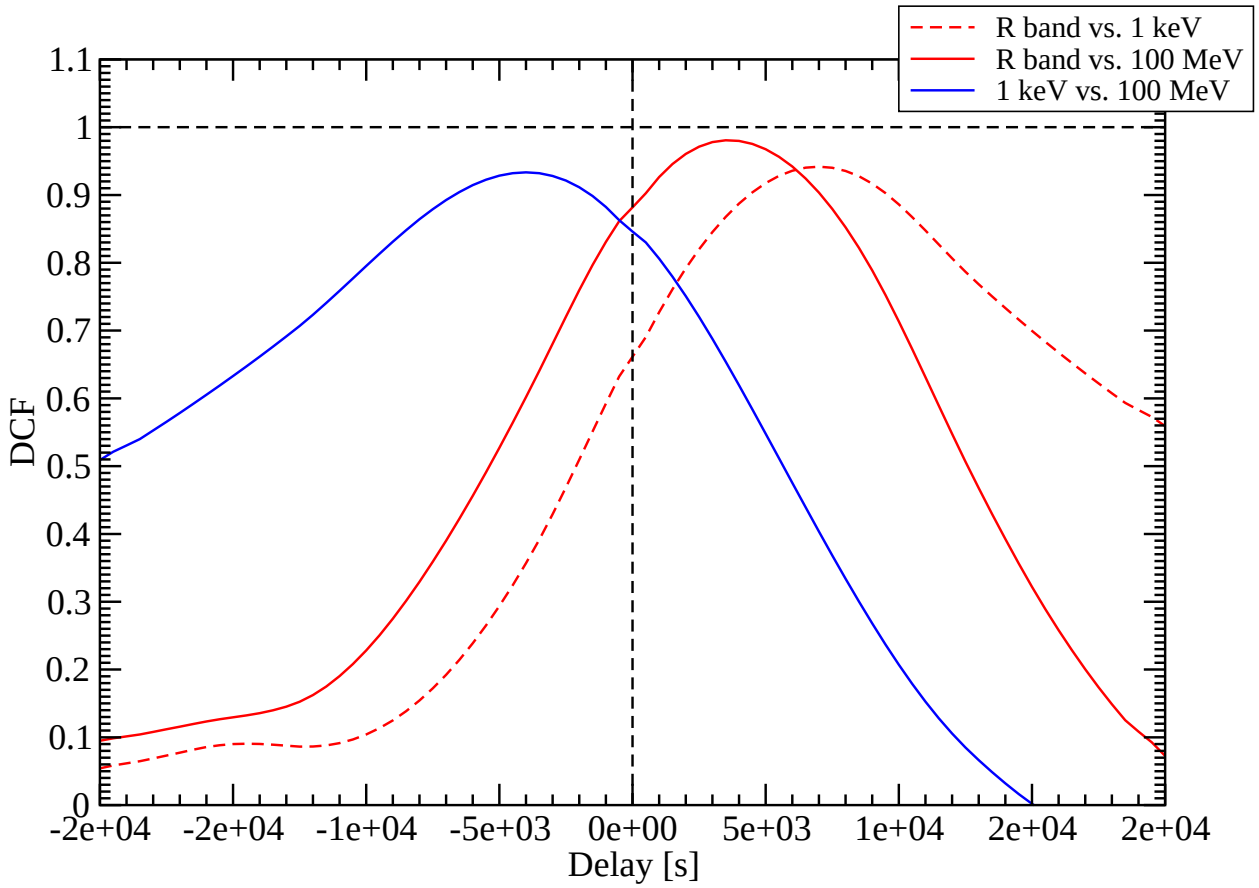


Fig. 4.— Discrete correlation functions between all energy bands for which light curves are plotted in Figure 3. A positive delay of "band 1 vs. band 2" indicates a lead of band 1 before band 2.

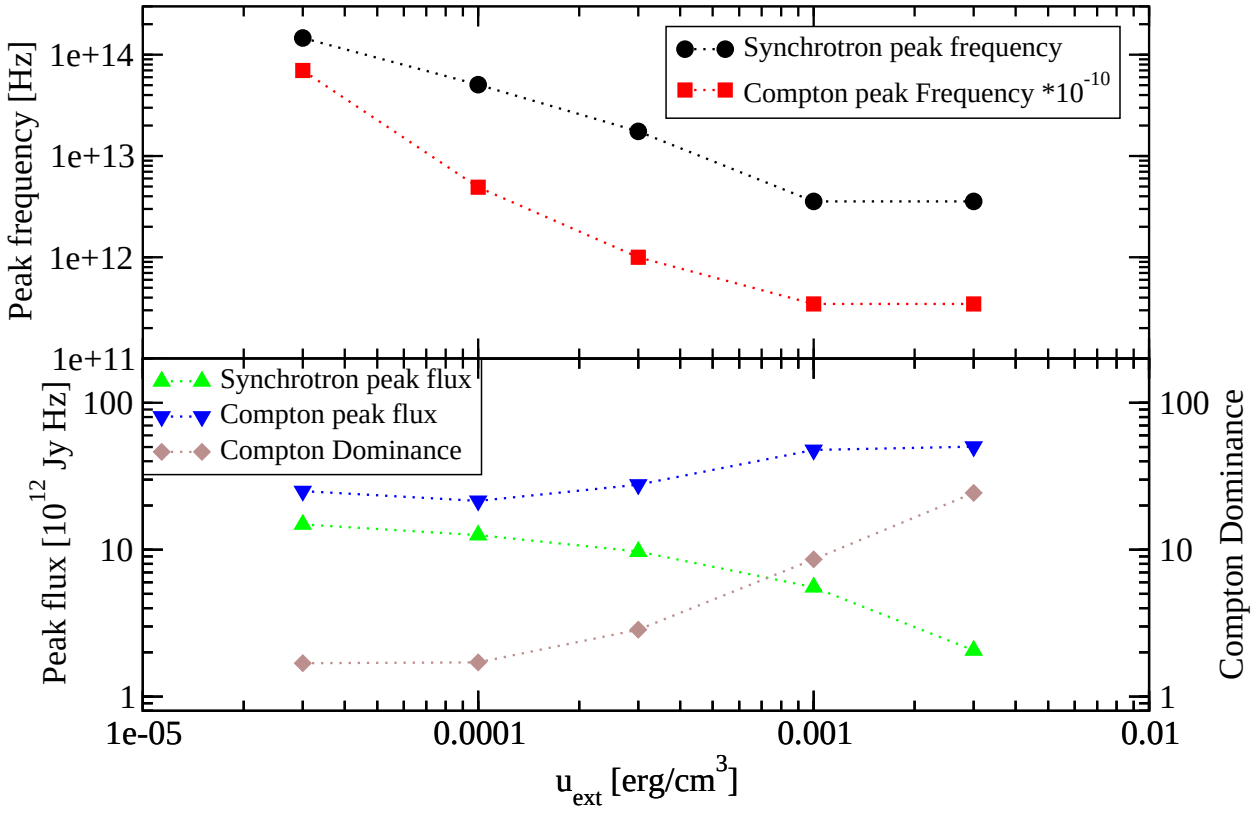


Fig. 5.— Characteristics of the time-averaged SED as a function of the external radiation energy density $u_{\rm ext}$.

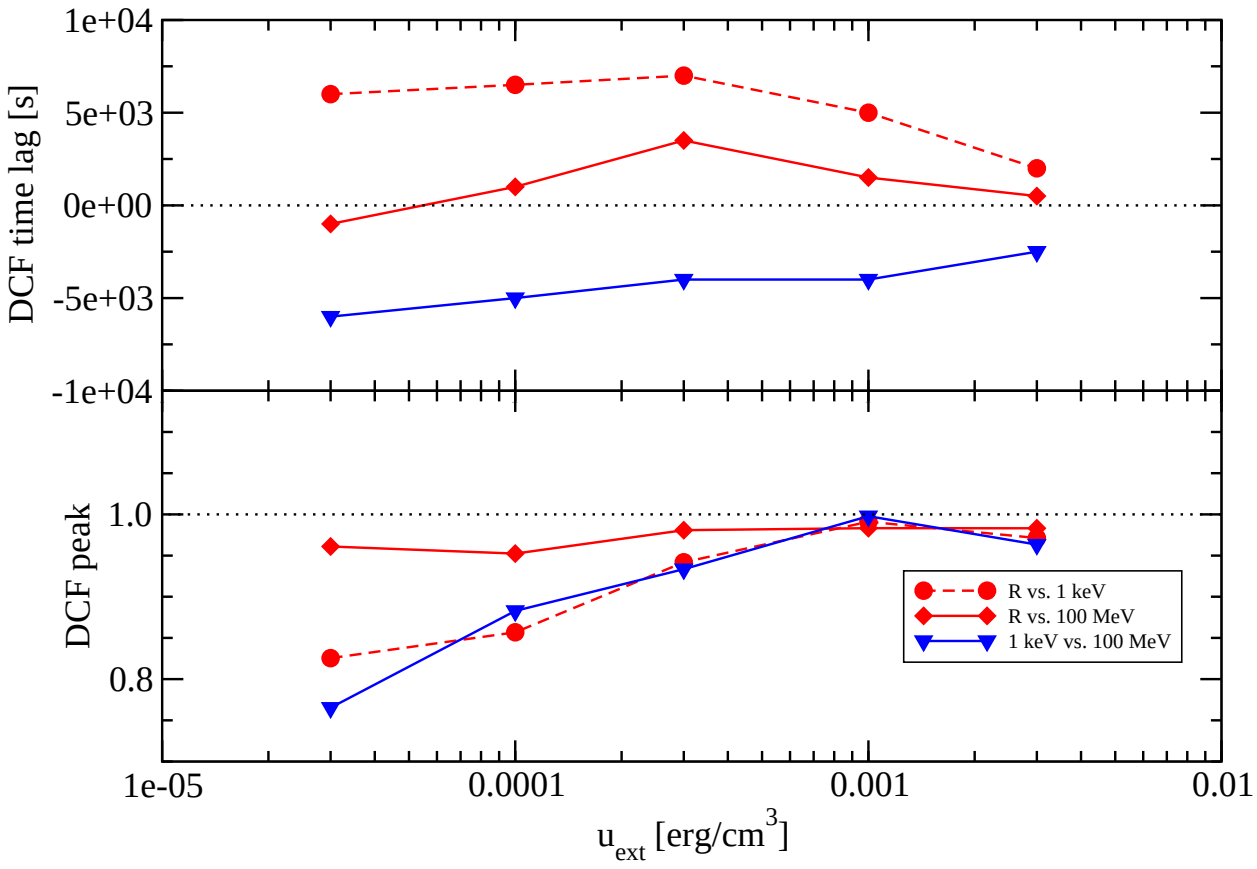


Fig. 6.— Characteristics of the DCFs as a function of the external radiation energy density $u_{\rm ext}$.

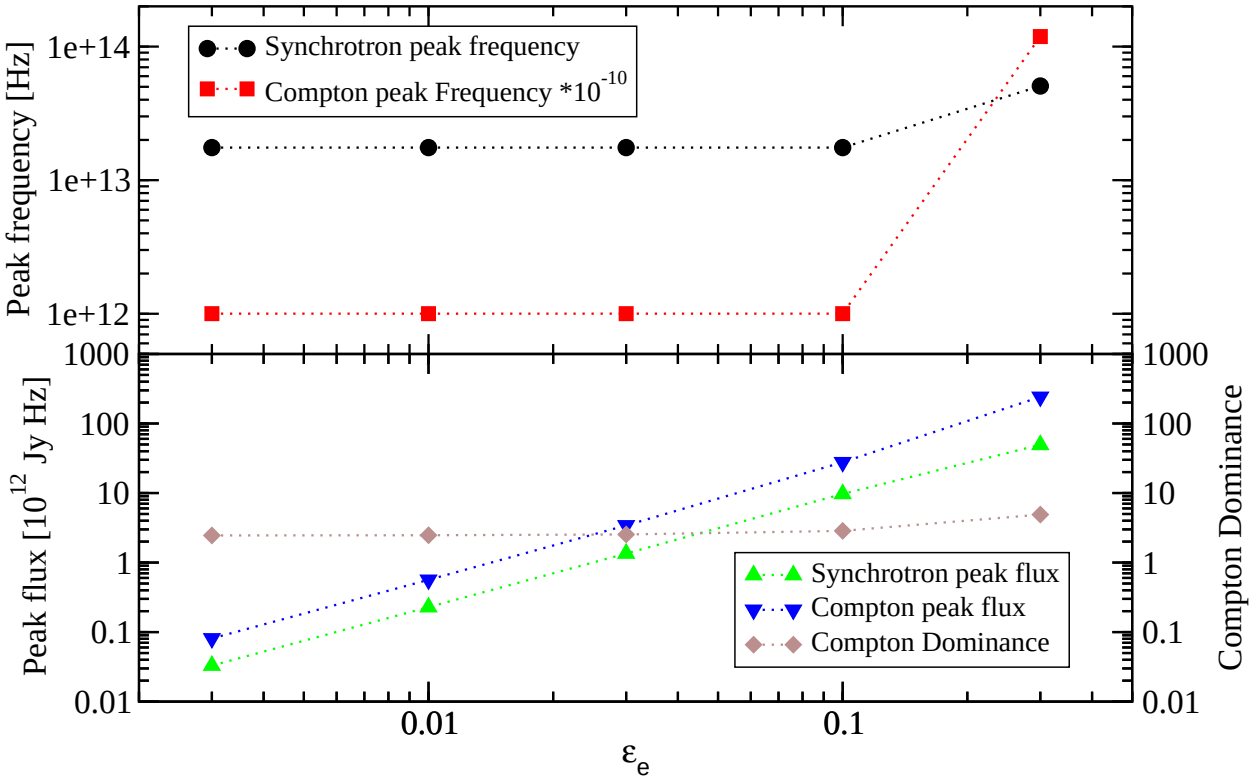


Fig. 7.— Characteristics of the SEDs as a function of the electron equipartition fraction ϵ_e.

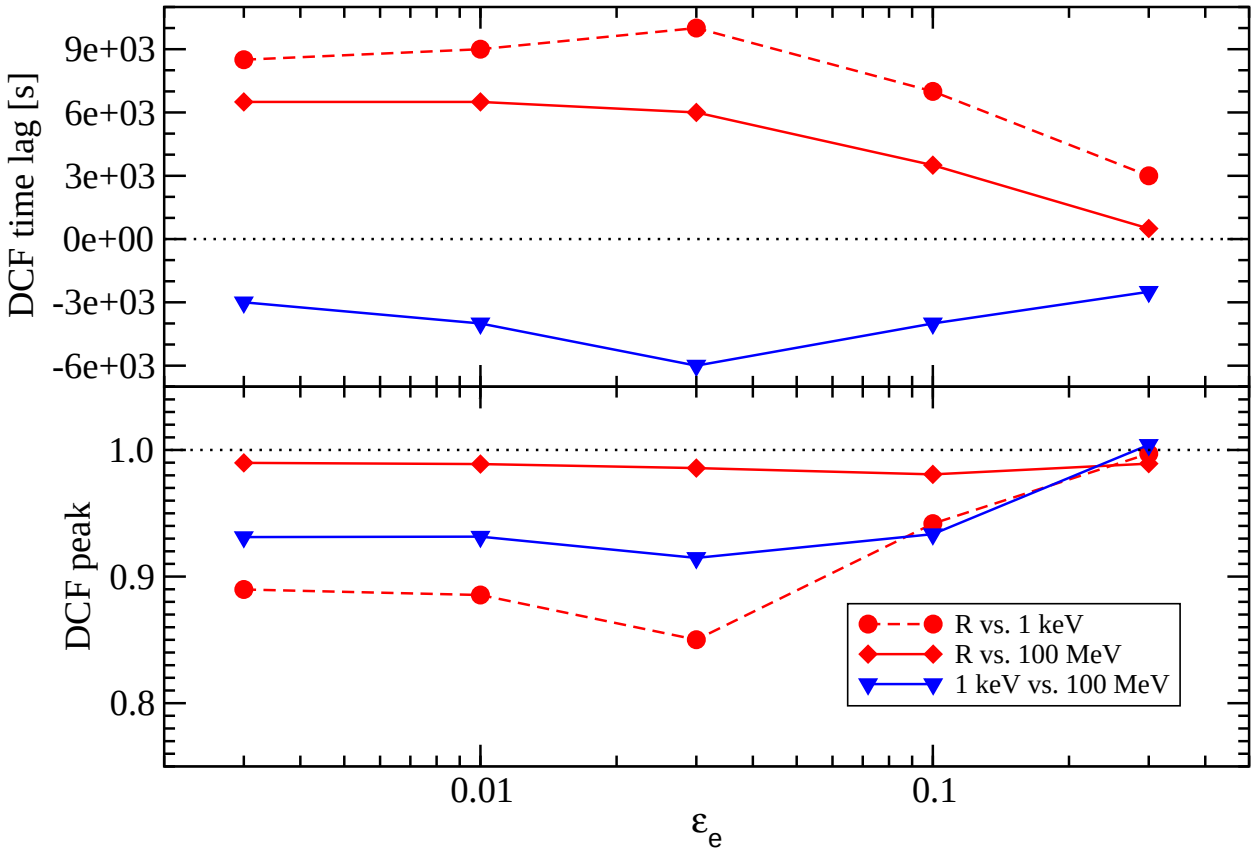


Fig. 8.— Characteristics of the DCFs as a function of the electron equipartition fraction ϵ_e.

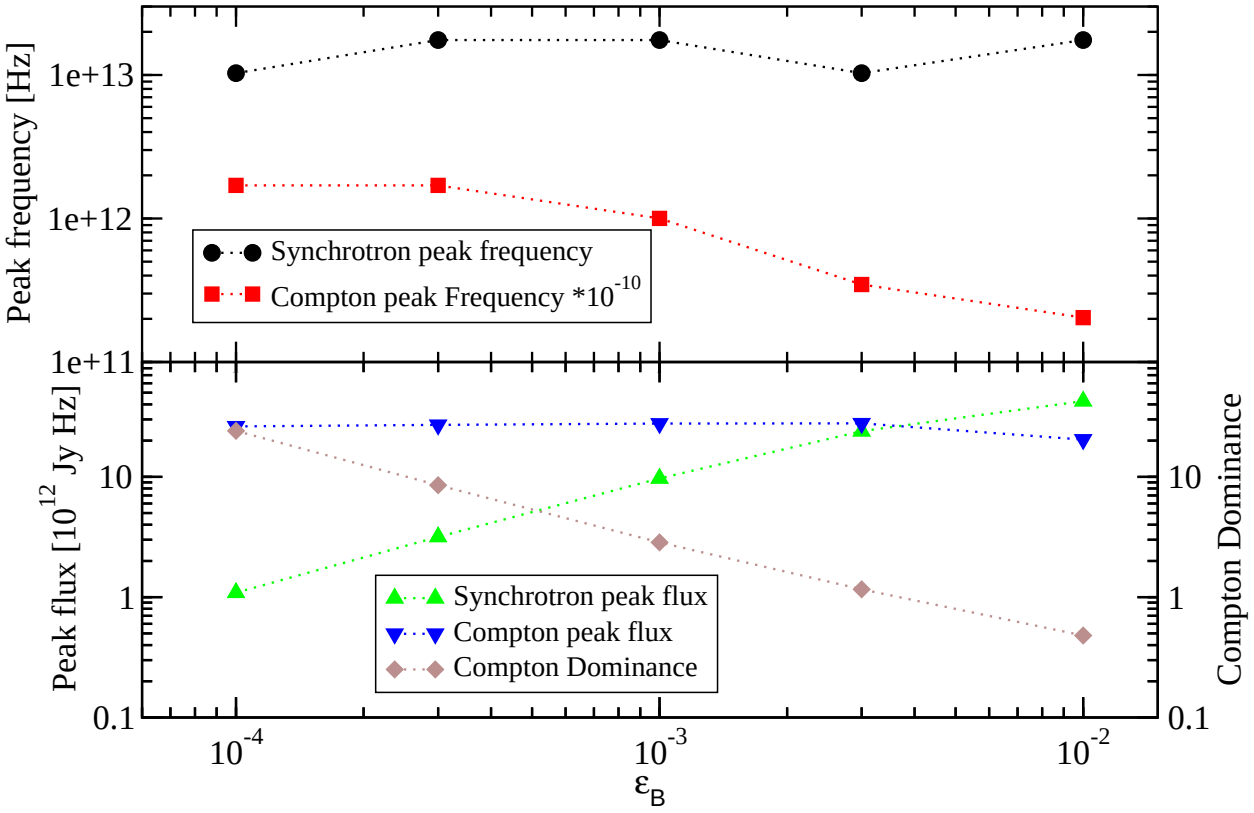


Fig. 9.— Characteristics of the SEDs as a function of the magnetic-field equipartition fraction ϵ_B.

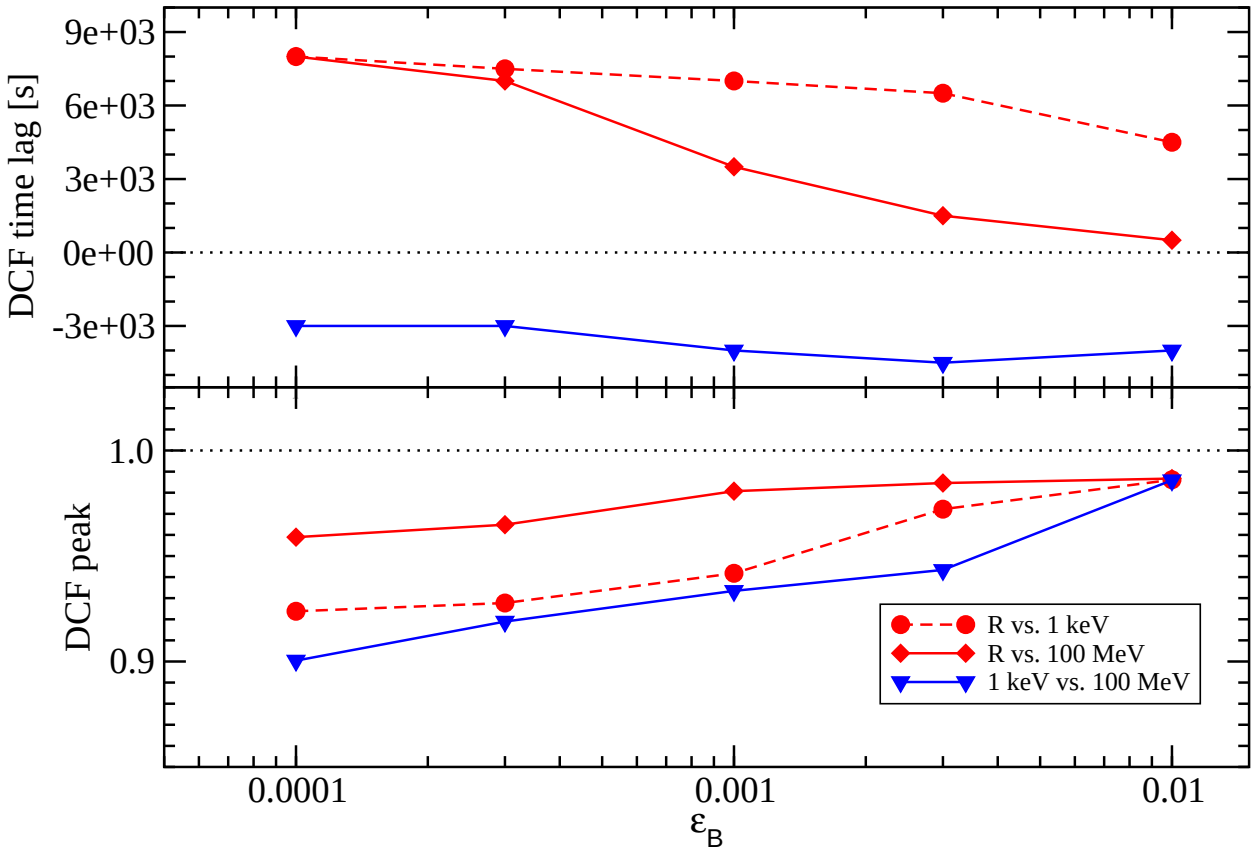


Fig. 10.— Characteristics of the DCFs as a function of the magnetic-field equipartition fraction ϵ_B.

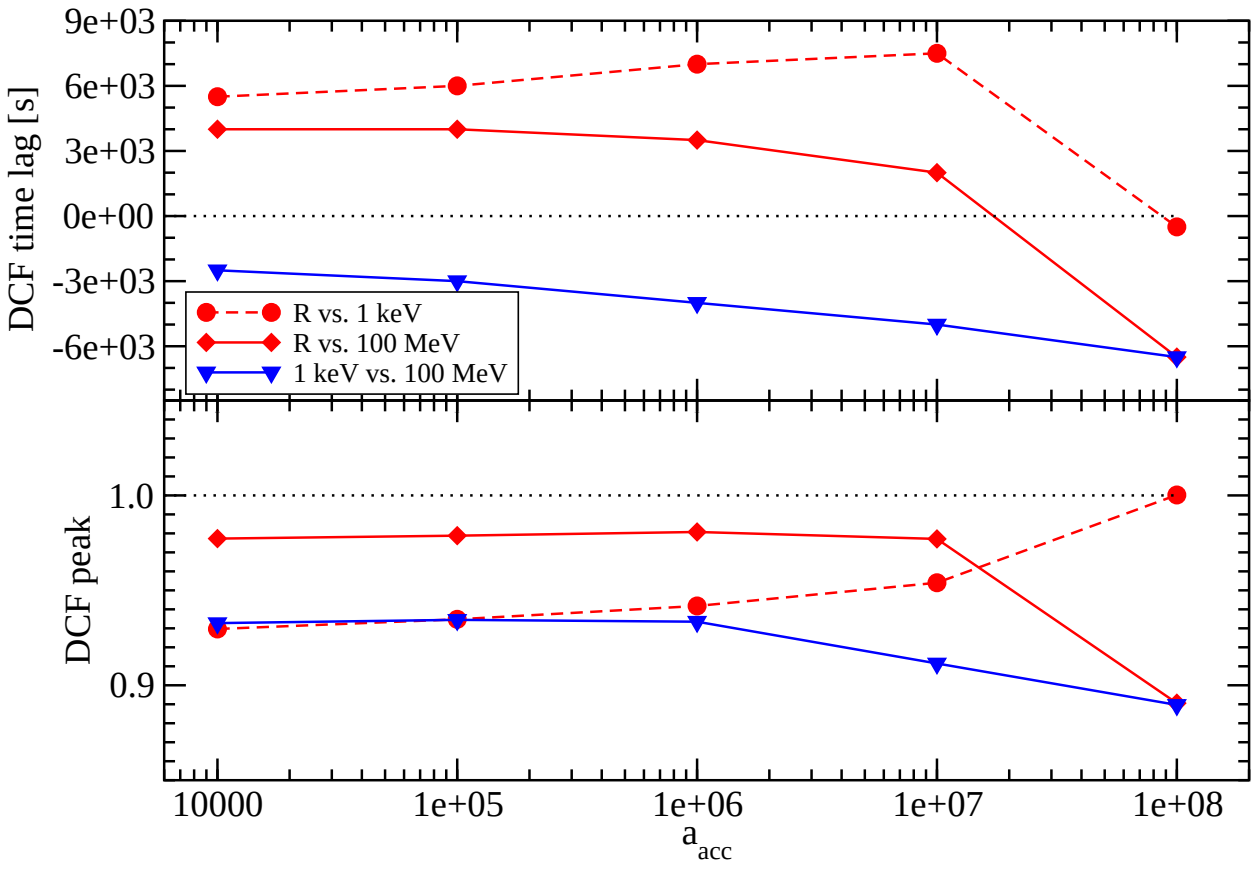


Fig. 11.— Characteristics of the DCFs as a function of the electron acceleration efficiency parameter $a_{\rm acc}$.

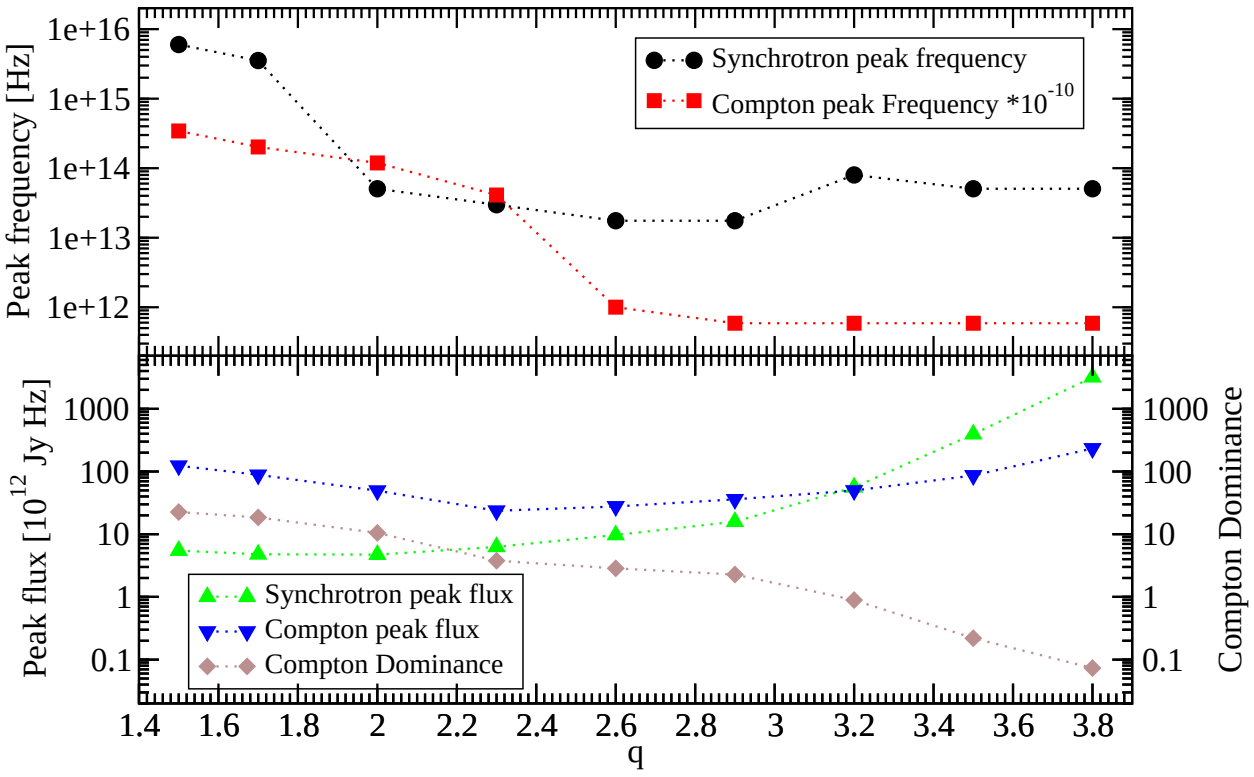


Fig. 12.— Characteristics of the SEDs as a function of the electron injection spectral index q.

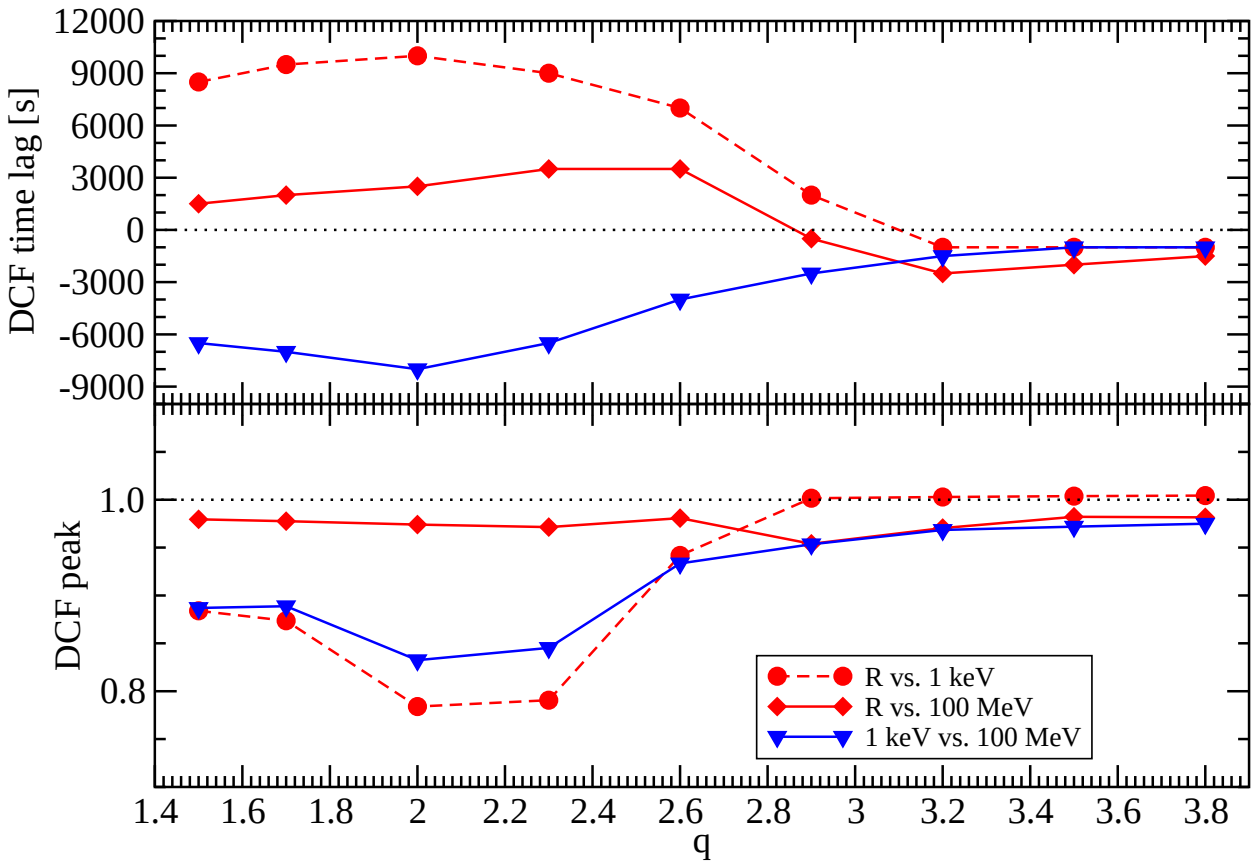


Fig. 13.— Characteristics of the DCFs as a function of the electron injection spectral index q.

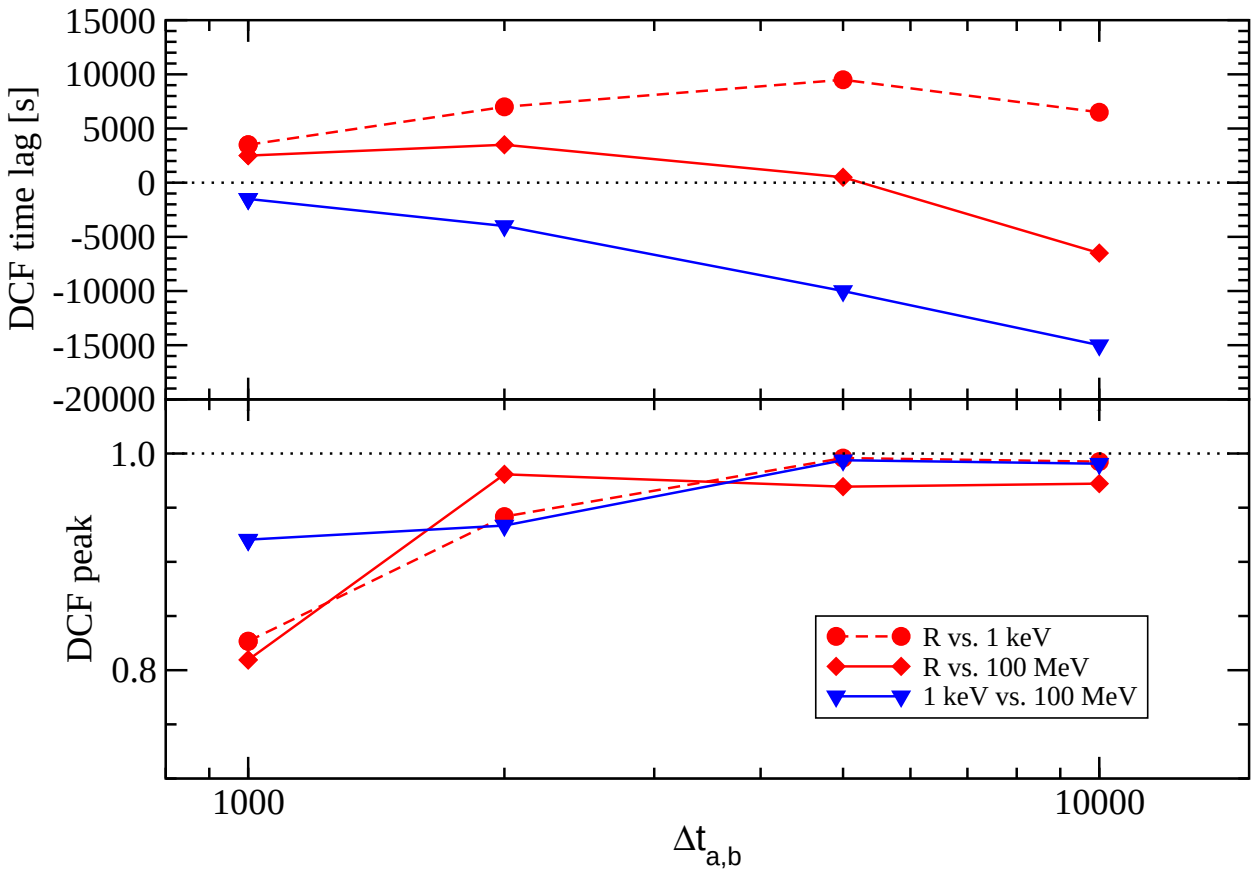


Fig. 14.— Characteristics of the DCFs as a function of the shell ejection time scales, $\Delta t_{\rm a,b}$

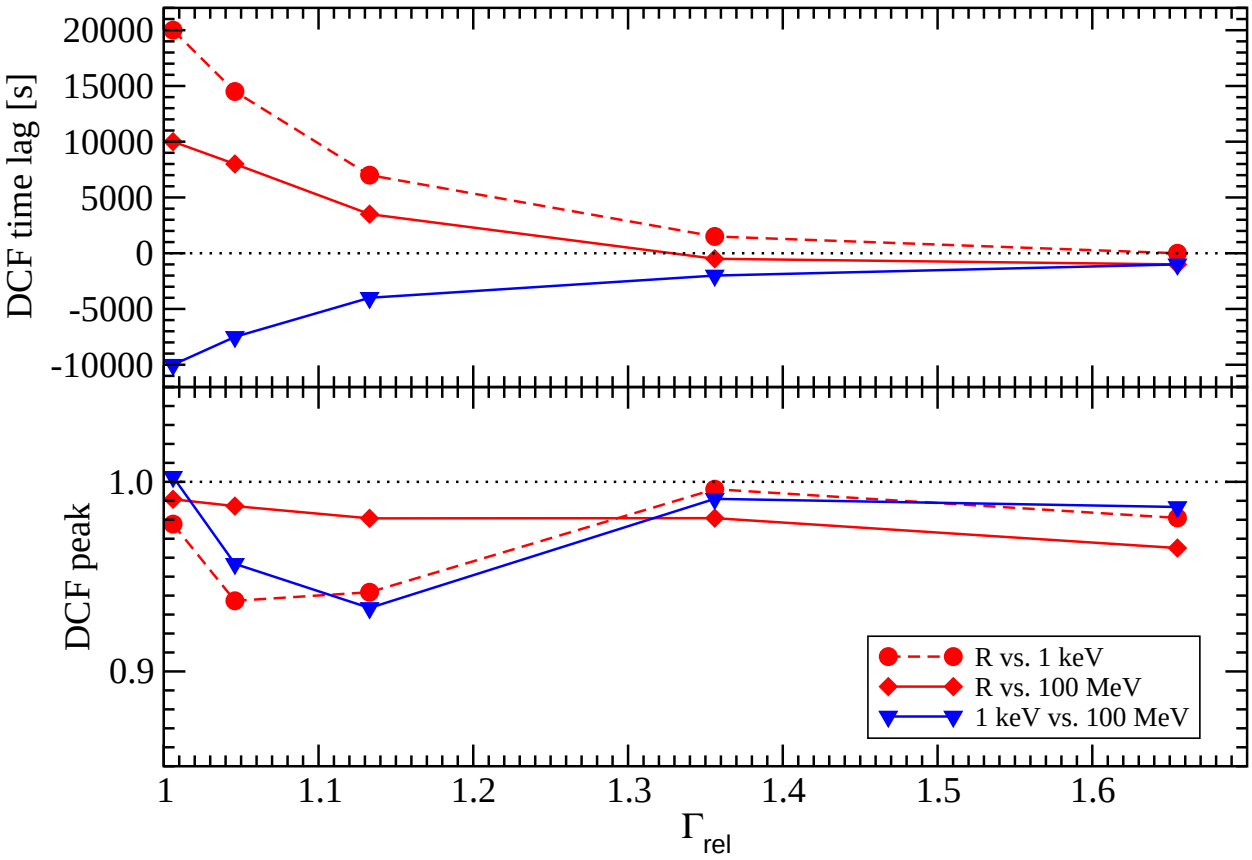


Fig. 15.— Characteristics of the DCFs as a function of the relative Lorentz factor between the shells, $\Gamma_{\rm rel}$.